Using spectral-based representative volume element crystal plasticity simulations to predict yield surface evolution during large scale forming simulations

Fengbo Han*, Martin Diehl, Franz Roters, Dierk Raabe

Max-Planck-Institut für Eisenforschung, Düsseldorf, Germany

ABSTRACT

We present a new approach to predict the evolution of anisotropic yield functions by coupling large scale forming simulations with crystal plasticity-spectral based virtual experiments, realizing a multi-scale model for metal forming. Employing a fast spectral method solver enables us to conduct on-the-fly full-field virtual experiments to evolve the yield surface at each integration point of the macroscopic finite element model. As illustrative example, two advanced anisotropic yield functions, namely Yld2000-2D and Yld2004-18p, are used in finite element simulations of deep drawing for a 2090-T3 aluminum alloy sheet. The simulated earing profiles are compared to the experimental ones as well as to simulations with non-evolving yield functions. It is found that the prediction of the earing is improved for the case of the evolving Yld2000-2D yield function. The evolution of the plastic anisotropy during cup drawing is systematically analyzed, showing that the evolution of anisotropy can have considerable effect on the prediction accuracy of the macroscopic simulations.

1. Introduction

Plastic anisotropy of polycrystalline metals, especially for sheet metals produced via complex thermo-mechanical treatments, is mainly controlled by the crystallographic texture. In metal forming simulations it is critical to take the texture-induced plastic anisotropy into consideration for achieving accurate simulations. Phenomenological yield functions that are usually used in large scale forming simulations and crystal plasticity (CP) models for mesoscale simulations are the two main approaches to describe the anisotropic plastic deformation behavior of polycrystalline metals.

Various advanced yield functions have been developed for different material classes since the first anisotropic yield function was proposed by Mises (1928). In 1948 Hill (1948) proposed a quadratic anisotropic yield function, which is especially suited for body centered cubic materials. Hosford (1972) proposed a non-quadratic isotropic yield function which he generalized to an anisotropic one later, c.f. Hosford (1979). Barlat and Lian (1989) further extended Hosford's approach to take into account planar anisotropy. In their work, a linear transformation method is used to keep the convexity of the yield function. Since then, such linear transformation based approach has established one of the most important branches of advanced yield functions. The stress invariants based approach is another important approach to anisotropic

yield functions, see for example Drucker (1949). Vegter et al. (2003) proposed a plane stress yield function by using second-order Bézier curves to interpolate discrete data points obtained from experiments. Van Houtte and Van Bael (2004) proposed a polynomial type yield function. Comsa and Banabic (2008) developed a plane stress yield function in the form of an expandable finite series. Recently, Raemy et al. (2017) proposed a planar Fourier series based yield function, which is very flexible. All these advanced yield functions show excellent ability to describe plastic anisotropy. Applications of these anisotropic yield functions have shown improved prediction accuracy in numerical simulations of various kinds of metal forming processes, e.g. cup drawing, stamping, hole expansion, and related spring back.

CP models based on different assumptions have shown good abilities in describing the mechanical response of polycrystalline metals. The first CP model was proposed by Sachs (1929) based on an iso-stress assumption, under which the resolved stress on the slip system with the highest resolved shear stress is assumed to be identical in all grains within the polycrystalline aggregate. Taylor (1938) developed the second CP model, known as the full-constraint (FC) model, which is based on an iso-strain assumption. Bishop and Hill (1951) proposed an equivalent solution method for the polycrystalline aggregate as the FC Taylor model, hence it was later named Taylor-Bishop-Hill (TBH) model. Due to the omission of grain-to-grain interactions, Taylor-type

models violate stress equilibrium. Trying to improve the FC Taylor model, various relaxed-constraint models were proposed, see for example Raphanel and Van Houtte (1985). To account for interactions among the grains in a polycrystalline aggregate, several kinds of grain cluster models were developed. Van Houtte et al. (1999) proposed the LAMEL model by treating two grains at a time. Furthermore, Van Houtte et al. (2005) developed the ALAMEL model that takes into account the stress equilibrium at grain boundaries. Raabe (1995) describes a grain interaction (GIA) model considering the orientation dependent interaction between neighboring grains. Tjahjanto et al. (2009) presented a relaxed grain cluster (RGC) model considering a cluster of eight or more hexahedral grains. The Visco-Plastic Self-Consistent (VPSC) approach developed by Lebensohn and Tomé (1993) is an homogenization scheme which takes the long-range interactions of grains into account by treating each grain as an ellipsoidal inclusion in a surrounding homogeneous equivalent medium that can be derived from the total grain ensemble and its texture.

Unlike these mean-field CP models, which incorporate the microstructure only in a statistical way, full-field CP models explicitly consider the microstructural morphology. In such models local grain interactions are captured, and the requirement of stress equilibrium at grain boundaries is satisfied as well as that of strain compatibility. Full-field CP models are usually solved either by employing a well-established Finite Element Method (FEM) solver or by employing a spectral solver based on Fast Fourier Transforms (FFTs). While the CP-FEM is flexible to deal with micromechanical problems of arbitrarily shaped geometries imposed with complex boundary conditions, the CP-FFT is more efficient for dealing with problems that are limited to periodic boundary conditions.

Limitations exist for both, anisotropic yield functions and CP models. As indicated by Roters et al. (2010), CP models need to be incorporated into the FEM via a homogenization approach when utilized in mechanical simulation of engineering structures. Such so-called embedded models are computationally very costly and often infeasible for practical applications. In contrast, anisotropic yield functions are very efficient when it comes to engineering forming scenarios. However, yield functions typically describe only the initial plastic anisotropy, which is a substantial limitation when a significant texture evolution occurs during deformation. The homogeneous anisotropic hardening (HAH) model proposed by Barlat et al. (2011) allows the yield surface to evolve when strain path changes.

To benefit from the accuracy of CP models, the calibration of yield functions can be done by CP-based virtual experiments as a substitute for mechanical tests. Barlat et al. (2005) identified the parameters of the Yld2004-18p by a combination of experimental data and the simulated out-of-plane stress points obtained from the VPSC model. Grytten et al. (2008) evaluated different combination strategies of experimental and Taylor model-based simulation data to identify the parameters of Yld2004-18p and suggested that more advanced CP models should be used in such approaches. Rabahallah et al. (2009) generated yield stress points for calibration of the plastic strain rate potential Srp2004-18p by utilizing the TBH model. Inal et al. (2010) employed a full-field CP model to replace mechanical tests for parameter identification of the CPB06ex2 yield criterion. An et al. (2011) proposed a yield locus description on the basis of the Taylor theory, and employed it to generate input data to calibrate the Yld2000-2D and BBC2005 yield functions. Saai et al. (2013) conducted CP-FEM simulations to obtain yield stress data needed for calibrations of Yld2004-18p for aluminum sheets with different textures. In the work by Zhang et al. (2015), the Facet yield surface was calibrated using stress data obtained from four kinds of CP models. The Yld2004-18p criterion was also calibrated in their work by three strategies, namely, by using uniaxial tensile data, 201 virtual yield stress points, and a combination of simulated data and experimental data, respectively. The authors found that the combination strategy can not only capture the experimental results but also fit the CP results well at the same time. Zhang

et al. (2014) also employed CP-FEM to generate yield stress points to calibrate the Yld2004-18p criterion. Recently, Zhang et al. (2016) conducted high resolution FFT-based CP simulations to obtain data to determine the initial yield surfaces represented by Yld91, Yld2000-2D, Yld2004-18p, and Yld2004-27p yield functions, showing an efficient virtual laboratory approach.

Instead of just focusing on the calibration of the initial yield surface, models that take into account the evolution of plastic anisotropy are also desired. Plunkett et al. (2006) established an evolution law for the anisotropic parameters of the yield function to enable shape change of the yield surface. The parameters involved in the CPB05 yield function at a series of equivalent plastic strain levels were pre-calibrated, and then interpolated at any strain level during the macroscopic simulation. This approach was also employed to describe the mechanical response of α-titanium by Nixon et al. (2010). Nevertheless, the approach of a simple interpolation is not suited to cover all possible strain paths encountered in complex forming operations.

Therefore, attempts have been made to integrate CP models in an adaptive way to conduct calibration for the anisotropic yield function on the fly, i.e. during the macroscopic simulation. Gawad et al. (2013) have demonstrated this approach by employing the Facet plastic potential in the macroscopic FEM simulation and the ALAMEL CP model in the microscale virtual experiments. In their works, the parameters of the Facet plastic potential for each integration point were updated by the ALAMEL-based virtual experiments when a certain upgrade criterion is reached. Gawad et al. (2015) extended the approach to allow the anisotropic plane-stress yield function BBC2008 to evolve during macroscopic simulation. He et al. (2014) applied the approach to describe the mechanical behavior of hexagonal materials using the CPB06ex2 yield function, where the VPSC model was employed for the virtual experiments. Kohar et al. (2019) used a Taylor-type CP model to calibrate the CPB06ex3 and CPB06ex5 yield functions in a multi-scale framework.

In this work we present a new approach to evolve advanced anisotropic yield functions in component-scale simulations with CP-spectral based virtual experiments. The new approach realizes a multi-scale model which allows macroscopic forming simulations to benefit from microscopic CP simulations for accurate description of the plastic anisotropy evolution. The paper is structured as follows: two advanced anisotropic yield functions are reviewed in Section 2. In Section 3, the backgrounds of the CP model and the spectral method are provided. Full details of the material and model set-up are given in Section 4. The results and discussions are presented in Section 5. A summary is provided in Section 6 along with an outlook for further work.

2. Advanced anisotropic yield functions

2.1. Yld2000-2D yield function

Barlat et al. (2003) defined the anisotropic plane stress yield function Yld2000-2D as

$$\Phi = |\tilde{S}_1' - \tilde{S}_2'|^n + |2\tilde{S}_2'' + \tilde{S}_1''|^n + |2\tilde{S}_1'' + \tilde{S}_2''|^n = 2\bar{\sigma}^n \qquad (1)$$

where $\tilde{S}_i'$ and $\tilde{S}_i''$ ($i = 1, 2$) are the principal values of the linearly transformed stress tensor $\tilde{\mathbf{s}}'$ and $\tilde{\mathbf{s}}''$ respectively, which are defined as

$$\tilde{\mathbf{s}}' = \begin{bmatrix} \alpha_1 & 0 & 0 \\ 0 & \alpha_2 & 0 \\ 0 & 0 & \alpha_7 \end{bmatrix} \begin{bmatrix} s_{11} \\ s_{22} \\ s_{12} \end{bmatrix},$$

$$\tilde{\mathbf{s}}'' = \frac{1}{3} \begin{bmatrix} 4\alpha_5 - \alpha_3 & 2\alpha_6 - 2\alpha_4 & 0 \\ 2\alpha_3 - 2\alpha_5 & 4\alpha_4 - \alpha_6 & 0 \\ 0 & 0 & 3\alpha_8 \end{bmatrix} \begin{bmatrix} s_{11} \\ s_{22} \\ s_{12} \end{bmatrix} \qquad (2)$$

where s_{11}, s_{22}, and s_{12} are the components of the deviatoric stress tensor $\tilde{\mathbf{s}}$. The eight anisotropy parameters (α_i, $i = 1 \ldots 8$) of this yield function can be identified from eight experimental anisotropic properties of the

sheet, namely σ_0, σ_{45}, σ_{90}, σ_b, r_0, r_{45}, r_{90} and r_b. Here σ denotes the yield stress and r the r-value. The index gives the angle to the rolling direction and b stands for bi-axial.

2.2. Yld2004-18p yield function

Barlat et al. (2005) proposed the Yld2004-18p function for the 3D stress case as

$$\Phi = |\tilde{S}_1' - \tilde{S}_1''|^n + |\tilde{S}_1' - \tilde{S}_2''|^n + |\tilde{S}_1' - \tilde{S}_3''|^n + |\tilde{S}_2' - \tilde{S}_1''|^n + |\tilde{S}_2' - \tilde{S}_2''|^n$$
$$+ |\tilde{S}_2' - \tilde{S}_3''|^n + |\tilde{S}_3' - \tilde{S}_1''|^n + |\tilde{S}_3' - \tilde{S}_2''|^n + |\tilde{S}_3' - \tilde{S}_3''|^n = 4\bar{\sigma}^n,$$

(3)

where $\tilde{S}_i'$ and $\tilde{S}_i''$ ($i = 1, 2, 3$) are the principal values of stress tensor $\tilde{s}'$ and $\tilde{s}''$ respectively, which are defined as

$$\tilde{s}' = \begin{bmatrix} 0 & -\alpha_1 & -\alpha_2 & 0 & 0 & 0 \\ -\alpha_3 & 0 & -\alpha_4 & 0 & 0 & 0 \\ -\alpha_5 & -\alpha_6 & 0 & 0 & 0 & 0 \\ 0 & 0 & 0 & \alpha_9 & 0 & 0 \\ 0 & 0 & 0 & 0 & \alpha_7 & 0 \\ 0 & 0 & 0 & 0 & 0 & \alpha_8 \end{bmatrix} \begin{bmatrix} s_{11} \\ s_{22} \\ s_{33} \\ s_{12} \\ s_{23} \\ s_{31} \end{bmatrix},$$

$$\tilde{s}'' = \begin{bmatrix} 0 & -\alpha_{10} & -\alpha_{11} & 0 & 0 & 0 \\ -\alpha_{12} & 0 & -\alpha_{13} & 0 & 0 & 0 \\ -\alpha_{14} & -\alpha_{15} & 0 & 0 & 0 & 0 \\ 0 & 0 & 0 & \alpha_{18} & 0 & 0 \\ 0 & 0 & 0 & 0 & \alpha_{16} & 0 \\ 0 & 0 & 0 & 0 & 0 & \alpha_{17} \end{bmatrix} \begin{bmatrix} s_{11} \\ s_{22} \\ s_{33} \\ s_{12} \\ s_{23} \\ s_{31} \end{bmatrix}$$

(4)

where s_{11}, s_{22}, s_{33}, s_{12}, s_{23}, and s_{31} are the stress components. This 3D yield function contains 18 anisotropy parameters (α_i, $i = 1\ldots18$), of which 14 parameters describe the in-plane properties and the others describe the out-of-plane properties of the sheet. Typically, the 18 parameters can be identified with uniaxial tension data (σ_0, σ_{15}, σ_{30}, σ_{45}, σ_{60}, σ_{75}, σ_{90}, r_0, r_{15}, r_{30}, r_{45}, r_{60}, r_{75}, r_{90}) in the RD-TD plane, balanced biaxial data (σ_b, r_b) in the RD-TD plane, stress data for 45° tension in the TD-ND and ND-RD plane, as well as stress data for simple shear in the TD-ND and the ND-RD plane.

3. Crystal plasticity model and spectral method

3.1. Crystal plasticity model

For finite strain CP modeling, the total deformation gradient $\mathbf{F}$ is typically multiplicatively decomposed into elastic and plastic components as

$$\mathbf{F} = \mathbf{F}_e \mathbf{F}_p$$

(5)

where $\mathbf{F}_p$ denotes the inelastic shear deformation due to slip in certain crystalline planes and directions, and $\mathbf{F}_e$ accounts for rigid body rotation and elastic distortion of the crystal lattice. The plastic velocity gradient $\mathbf{L}_p$ is expressed as

$$\mathbf{L}_p = \dot{\mathbf{F}}_p \mathbf{F}_p^{-1} = \sum_{\alpha=1}^{N} \dot{\gamma}^\alpha \mathbf{s}_0^\alpha \otimes \mathbf{n}_0^\alpha$$

(6)

where $\dot{\gamma}^\alpha$ is the shear rate on the αth slip system represented by two unit vectors $\mathbf{s}_0^\alpha$ (slip direction) and $\mathbf{n}_0^\alpha$ (slip plane normal) in the crystal coordinate system. N is the number of slip systems. The plastic flow on a slip system is described by a rate dependent flow law as

$$\dot{\gamma}^\alpha = \dot{\gamma}_0 \left| \frac{\tau^\alpha}{g^\alpha} \right|^{1/m} \mathrm{sgn}(\tau^\alpha)$$

(7)

where $\dot{\gamma}_0$ is the reference strain rate, τ^α is the resolved shear stress, g^α is the slip resistance, and m is the strain rate sensitivity exponent. The evolution of g^α is given by

$$\dot{g}^\alpha = \sum_{\beta=1}^{N} h^{\alpha\beta} \dot{\gamma}^\beta$$

(8)

where $h^{\alpha\beta}$ is referred to as the hardening matrix, and is described by a saturation-type law as

$$h^{\alpha\beta} = h_0 [q + (1-q)\delta^{\alpha\beta}] \left| 1 - \frac{g^\beta}{g_\infty} \right|^a \mathrm{sgn}\left(1 - \frac{g^\beta}{g_\infty}\right)$$

(9)

where g_∞, h_0, a and q are the saturation values of the slip resistance, the reference self-hardening coefficient, the hardening exponent, and the latent hardening parameter, respectively. The latent hardening parameter is set to $q = 1.0$ for coplanar slip systems and $q = 1.4$ for non-coplanar slip systems (Peirce et al., 1982).

3.2. Spectral method

In this work, a large-strain spectral method implemented in DAMASK (Roters et al., 2019) is used to solve for mechanical equilibrium on a volume element with periodic boundary conditions. The details of this method can be found in the studies of Eisenlohr et al. (2013) and Shanthraj et al. (2015). In general, the spectral method outperforms FEM in the case of regular RVEs.
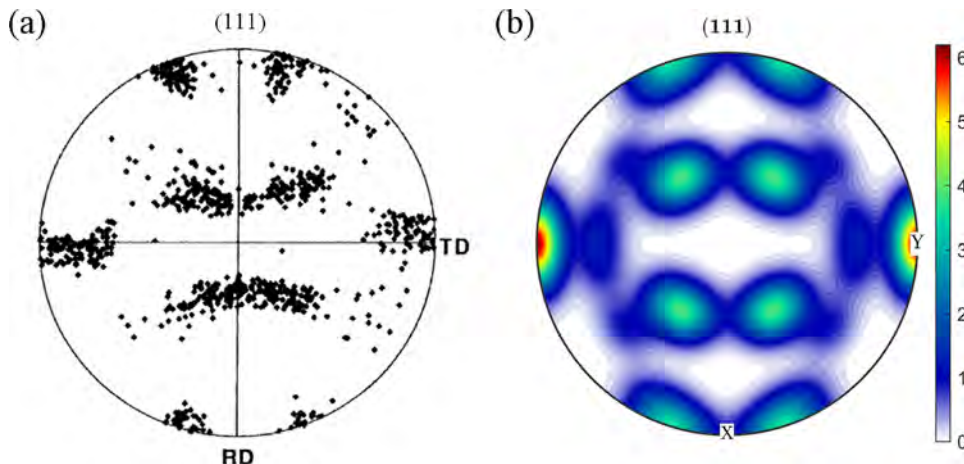

Fig. 1. Texture at the central layer of the 2090-T3 sheet (a) experiment (Rousselier et al., 2009) (b) reconstructed. ODF Kernel: von Mises-Fisher. Half-width: 10°.
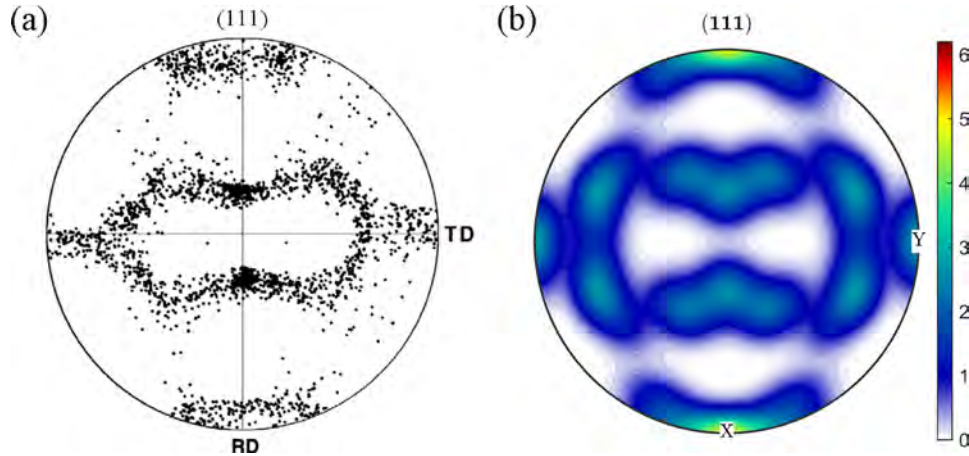
Fig. 2. Texture of the complete 2090-T3 sheet (a) experiment (Rousselier et al., 2009) (b) reconstructed. ODF Kernel: von Mises-Fisher. Half-width: 10°.

4. Material and model set-up

4.1. Initial texture

In this work, a novel multi-scale model is used to simulate the deformation of a strongly anisotropic 2090-T3 Al-Li alloy sheet with the thickness of 1.6 mm (Yoon et al., 2000). This sheet material contains a characteristic rolling texture, which is composed of S, Brass and Copper texture components (Rousselier et al., 2009), and has a texture gradient in the sheet thickness direction (Barlat et al., 1992). Figs. 1 and 2 show the {111} pole figures of the central layer texture and the complete texture of the sheet material in the TD-RD plane, respectively. The experimental pole figures are adopted from (Rousselier et al., 2009). The MTEX software (Bachmann et al., 2010) was utilized to reconstruct the orientation distribution functions (ODFs) of the central layer texture and complete texture. For the central layer texture, the Copper texture component is not present, and the reconstruction with a combination of S component with a volume fraction of 34.44% and Brass component with a volume fraction of 65.56% (Rousselier et al., 2009) shows good agreement with the experimental texture. For the complete texture, the reconstruction with a combination of S component (32%), Brass component (30%), and Copper component (38%) shows good agreement with the experimental texture. It needs to be noted that an calibrated (S) texture component ($\varphi_1 = 66.7093$, $\Phi = 22.3072$, $\varphi_2 = 44.0052$)

and (Brass) texture component ($\varphi_1 = 37.8371$, $\Phi = 39.4428$, $\varphi_2 = 0.3147$) from Rousselier et al. (2009) are used in the ODF reconstructions instead of the ideal S texture component ($\varphi_1 = 60$, $\Phi = 32$, $\varphi_2 = 65$) and Brass texture component ($\varphi_1 = 35$, $\Phi = 40$, $\varphi_2 = 0$).

4.2. Representative volume elements

The CP-spectral based virtual experiments need to provide anisotropic properties of the sheet material for the parameter identification of the yield functions, so two representative volume elements (RVEs) were created to represent the sheet metal. Fig. 3 shows the two RVEs that consist of $10 \times 10 \times 10$ Fourier points. Each Fourier point in the RVEs represents a grain. Euler angles sampled from the reconstructed ODFs for both textures by MTEX are assigned to the RVEs as illustrated in Fig. 3.

4.3. Material parameters

A genetic algorithm (Lin and Yang, 1999) based inverse optimization approach was utilized to identify the parameters of the CP constitutive model. Only the uniaxial tensile curve in RD was used in the optimization. Two fittings for both the central layer texture and complete texture were conducted, and the fitted parameters are listed in
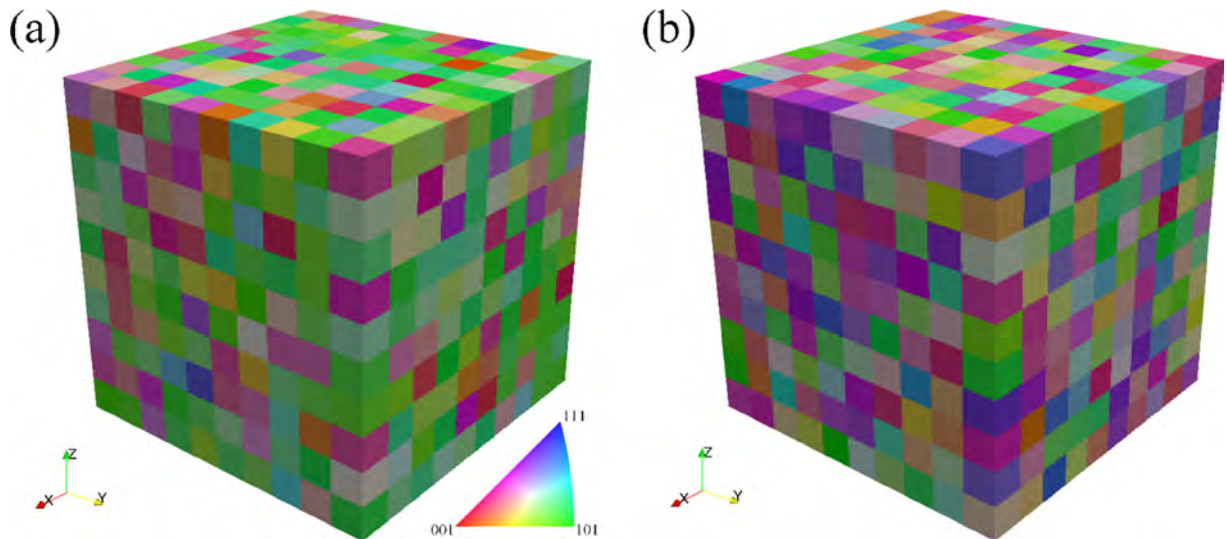

Fig. 3. Representative volume elements colored with the normal direction inverse pole figure (a) assigned with central layer texture (b) assigned with complete texture. RD//X-axes, TD// Y-axes, and ND//Z-axes.

Table 1
Parameters for the crystal plasticity model of the 2090-T3 aluminum alloy.

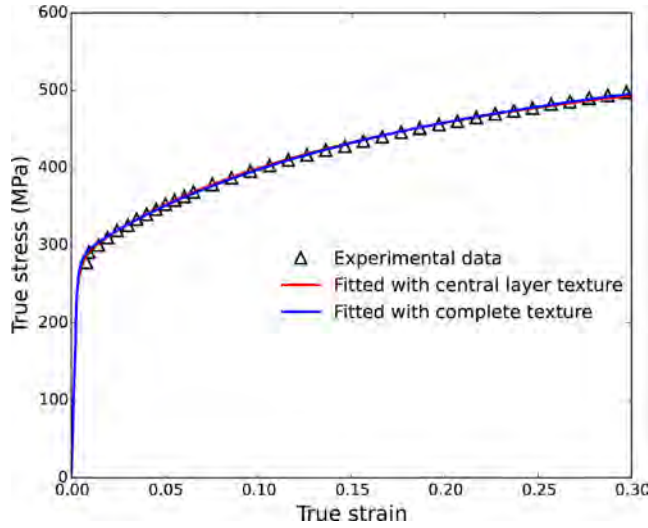| Texture	g_0 (MPa)	g_∞ (MPa)	h_0 (MPa)	a	$\dot{\gamma}_0$ (s^{-1})	m
Central layer texture	110.2	203.5	1000.7	1.97	0.001	0.02
Complete texture	106.5	214.5	749.9	2.19		

Fig. 4. Experimental and fitted stress-strain curves in RD. Experimental data is taken from (Rousselier et al., 2009).

Table 1. Fig. 4 shows the comparison between the fitted stress-strain curves and the experimental one. Both the fittings match very well with the experimental one, although the fitted parameters for the central layer texture and the complete texture are slightly different.

In the macroscale simulations, the same isotropic hardening model $\sigma = 646(0.025 + \varepsilon_p)^{0.227}$ (Rousselier et al., 2009) is used.

4.4. Virtual experiments

The virtual experiments are based on the fast and efficient spectral solver included in DAMASK (Roters et al., 2019). For example, it takes just 5 s to reach the yield point (at a plastic strain of 0.002) for a uni-axial tensile simulation (grid size = 10 × 10 × 10) using four threads on a workstation with Intel Xeon E5-2687W CPUs. The DAMASK si-mulation stops and returns the stress tensor and plastic strain rate tensor when the yield condition is satisfied.

To calibrate the Yld2000-2D yield function, virtual tensile tests along 0°, 45° and 90° relative to rolling direction and the balanced biaxial tensile test are conducted to obtain eight data points (σ_0, σ_{45}, σ_{90}, σ_b, r_0, r_{45}, r_{90} and r_b). Eight equations can be constructed to satisfy the yield stress and Lankford value, and the eight parameters (α_i, $i = 1...8$) for Yld2000-2D can be determined simultaneously using a Newton-Raphson scheme.

For the parameter identification of Yld2004-18p, virtual tensile tests along 0°, 15°, 30°, 45°, 60°, 75°, and 90° relative to the rolling direction, a balanced biaxial tensile test in the RD-TD plane, 45° tensile tests in the TD-ND and ND-RD plane, as well as simple shear tests in the TD-ND and ND-RD planes are conducted. The 18 parameters are optimized with the error function recommended by Barlat et al. (2005) as follows

$$R(\alpha_i) = \sum_p w_p \left(\frac{\sigma_p^{pre}}{\sigma_p^{vex}} - 1 \right)^2 + \sum_q w_q \left(\frac{r_p^{pre}}{r_p^{vex}} - 1 \right)^2 \tag{10}$$

where p denotes the number of stress data points obtained from the virtual tests, and q denotes the number of r-values. The superscript vex denotes the value obtained from virtual experiments, and pre denotes the predicted value. The weight coefficients w for the in-plane yield stresses and uniaxial r-values, and the other stresses are set to 1.00, 0.10 and 0.01, respectively (Barlat et al., 2005).

It should be noted that the virtual experiments and yield function calibration are conducted for each integration point of the macroscopic FE model adaptively. During the FE simulation, the local deformation gradient history is passed to DAMASK for calculating the new texture once the local accumulated plastic point exceeds 0.05 since the last update of the yield surface. After that, the virtual experiments are conducted based on the new texture to obtain the new plastic aniso-tropy data, then the yield functions are re-calibrated using the updated data. Therefore, the yield surface evolution at each integration point depends on the local texture evolution induced by plastic deformation.

4.5. FEM model for cup drawing

The Yld2000-2D and Yld2004-18p yield functions were im-plemented as a material subroutine for the FEM software ABAQUS/ Explicit. The geometrical setting of the cup drawing model is depicted in Fig. 5(a). Considering the orthotropic symmetry of the sheet, only a quarter of the blank is simulated. Fig. 5(b) shows the mesh of the blank. For simulations in conjunction with the plane stress yield function Yld2000-2D, the blank mesh contains 24 reduced integration wedge continuum shell elements (SC6R) and 624 reduced integration hex-ahedral continuum shell elements (SC8R) in one layer and 3 integration points in the thickness direction. For simulations with the full 3D yield
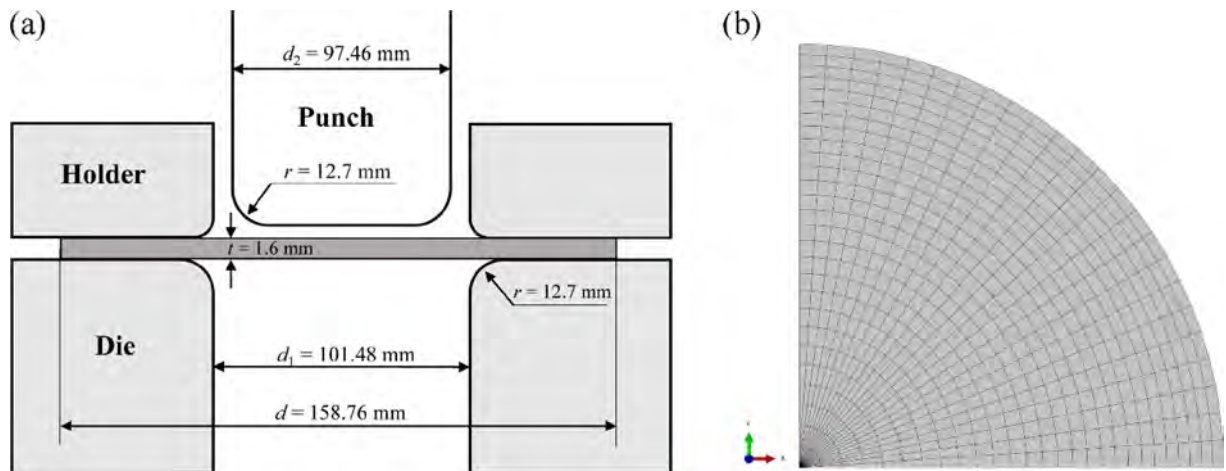

Fig. 5. Set-up of the cylindrical cup drawing model (a) Geometrical setting (b) mesh of the blank.
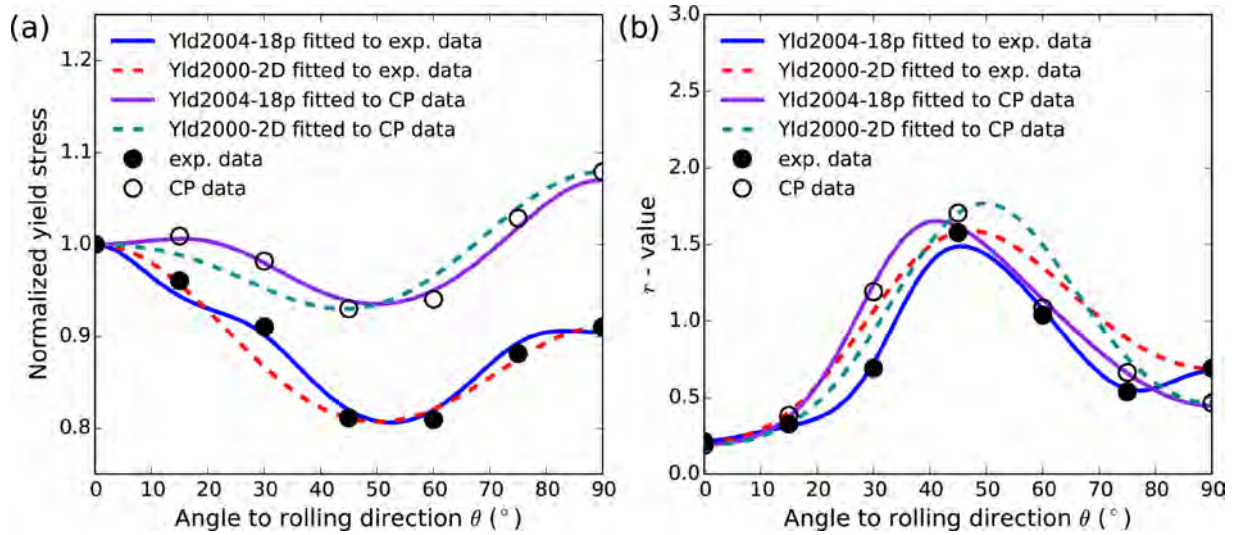
Fig. 6. Plastic anisotropy of the central layer texture (a) Normalized yield stress versus θ (b) r-value versus θ.
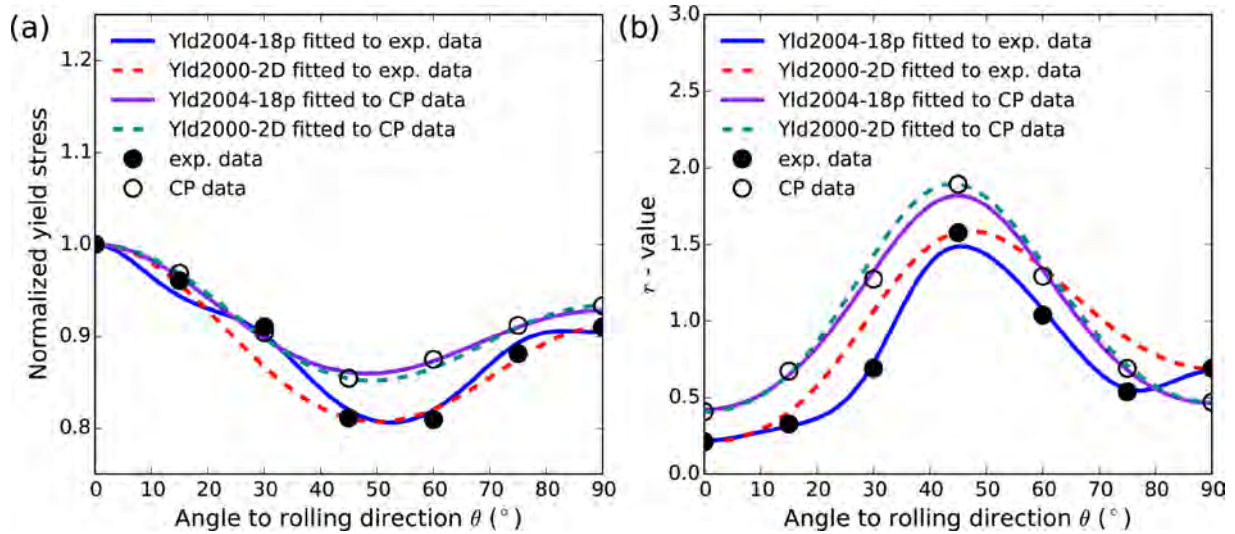

Fig. 7. Plastic anisotropy of the complete texture (a) Normalized yield stress versus θ (b) r-value versus θ.

Table 2
Average errors between the CP data and the experimental data.

	Error of normalized yield stresses	Error of r-values
Central layer texture	11.28%	24.26%
Complete texture	2.99%	55.44%

function Yld2004-18p, the blank was discretized in 3 layers with the same mesh, and it includes 72 wedge elements (C3D6) and 1872 reduced integration hexahedral elements (C3D8R). The default hourglass control algorithm of ABAQUS was adopted for both the shell elements and the solid elements. The holding force is 5.55 kN for the quarter region. The friction coefficient is set to 0.005 and no strain rate dependency is assumed.

5. Results and discussions

5.1. Initial plastic anisotropy

The data points in Figs. 6 and 7 show the comparison of the anisotropy of the normalized uniaxial yield stresses and r-values obtained from virtual tests for the two textures to those from experimental tests.

The yield stress data obtained from the CP model for the central layer texture presented in Fig. 6(a) shows a relatively large deviation from the experimental data. The highest yield stress value appears in RD for the experimental data, while that of the CP data for the central layer texture appears in TD. However, the profile of the r-values obtained from the CP model for the central layer texture (Fig. 6(b)) shows a good agreement with the profile of experimental r-values. The yield stress data obtained from the CP model for the complete texture (Fig. 7(a)) is much closer to the experimental data than that of the central layer texture, and the corresponding profile of r-values (Fig. 7(b)) is still in good agreement with the profile of experimental r-values, although the match is not as good as for the central layer texture. The average errors between the anisotropy data obtained from the CP model and the experimental data are listed in Table 2, from which a more quantitative comparison between the two textures can be obtained. Overall, the virtual tests with the CP model can serve as an accurate substitute for the elaborated mechanical tests required to determine the plastic anisotropy.

The lines in Figs. 6 and 7 show the plastic anisotropy predictions of Yld2000-2D and Yld2004-18p. The identified parameters for the yield functions are listed in Table 3. The agreement of the two yield functions to both the experimental data and the CP data is rather good, indicating

Table 3
Parameters identified for the Yld2004-18p and Yld2000-2D yield functions (exponent $n = 8$).

	Yld2004-18p			Yld2000-2D		
	Fitted to experimental data	Fitted to CP data		Fitted to experimental data	Fitted to CP data	
		central layer texture	complete texture		central layer texture	complete texture
α_1	−0.12970	1.05665	0.87383	0.48503	0.76681	0.75099
α_2	0.87322	0.84818	0.92538	1.37865	0.97366	1.19401
α_3	0.09478	0.88400	0.87358	0.75339	1.15032	1.22384
α_4	1.08173	1.44213	0.86837	1.02471	0.99681	1.12565
α_5	0.65084	1.52536	0.82882	1.03632	1.05496	1.02995
α_6	1.36157	0.77403	1.02153	0.90357	0.99973	0.94464
α_7	1.01840	1.26285	0.99848	1.23214	1.10717	1.20690
α_8	1.06505	1.25638	1.00000	1.48575	1.02565	1.15794
α_9	0.99237	1.70649	1.18384	–	–	–
α_{10}	1.01005	0.90811	0.78595	–	–	–
α_{11}	0.54935	1.45590	0.88135	–	–	–
α_{12}	0.56562	1.35593	1.10347	–	–	–
α_{13}	0.86620	1.22263	1.25872	–	–	–
α_{14}	1.09346	0.87599	1.22627	–	–	–
α_{15}	−0.20520	1.34045	0.90128	–	–	–
α_{16}	1.04630	1.24982	0.99848	–	–	–
α_{17}	1.14316	1.25882	1.00000	–	–	–
α_{18}	1.33495	1.12779	1.13962	–	–	–

that the plastic anisotropy of the material can be well reproduced when mapping it from the CP model to the yield functions. As Yld2004-18p is more flexible than Yld2000-2D, more details of the plastic anisotropy are captured by the former function. It needs to be noted that experimental anisotropy data for the fitting actually are combinations of experimental in plane data and calculated out-of-plane data, which are all taken from (Barlat et al., 2005, 2003).

Fig. 8 shows the yield surfaces predicted by the two yield functions identified with the experimental data. Due to the strong texture of this material, the yield surfaces exhibit a distorted shape. Figs. 9 and 10 show the yield surfaces predicted by the yield functions identified with

the CP data for the central layer texture and complete texture, respectively. The yield surfaces shown in Figs. 9 and 10 are not as distorted as that shown in Fig. 8. This can be ascribed to fact that we neglected the texture gradient of the sheet in the CP model (Tikhovskiy et al., 2006).

5.2. Simulations of the cup drawing test

We performed three groups of cup drawing simulations. In the first group, the yield functions were calibrated with the experimental data. In the second group, the yield functions were calibrated with the CP data. The parameters of Yld2000-2D and Yld2004-18p listed in Table 3
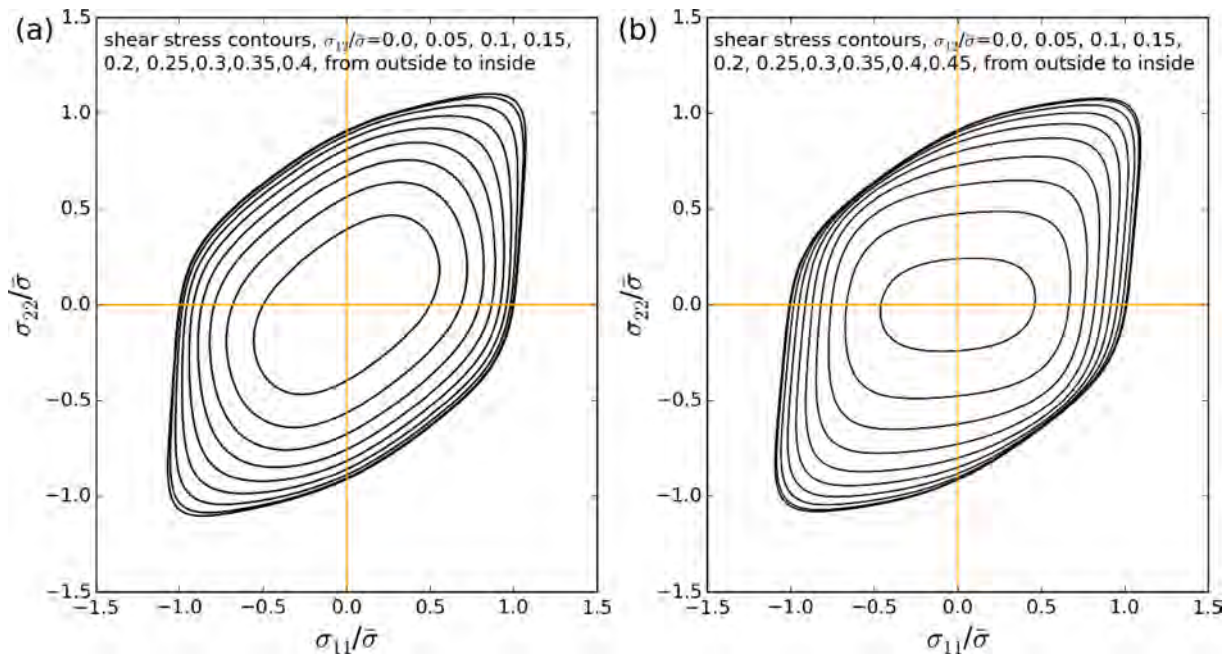

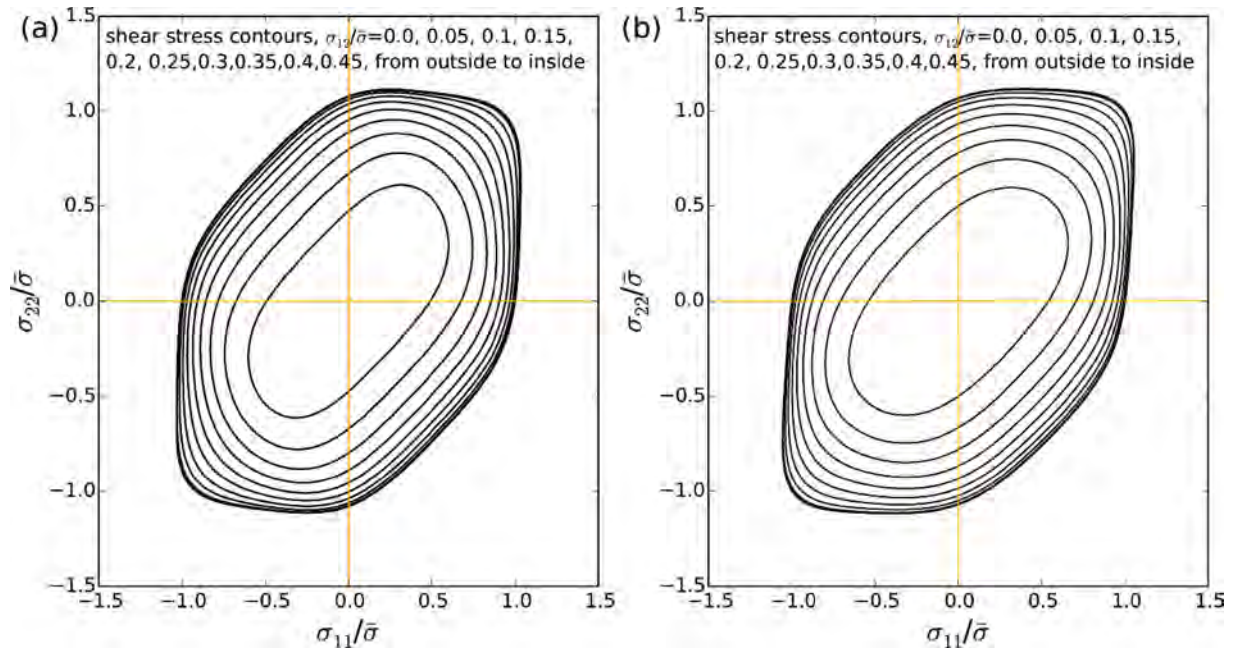**Fig. 8.** Yield surfaces obtained by fitting to experimental data (a) Yld2000-2D (b) Yld2004-18p.

Fig. 9. Yield surfaces obtained for central layer texture by fitting to the CP data (a) Yld2000-2D (b) Yld2004-18p.
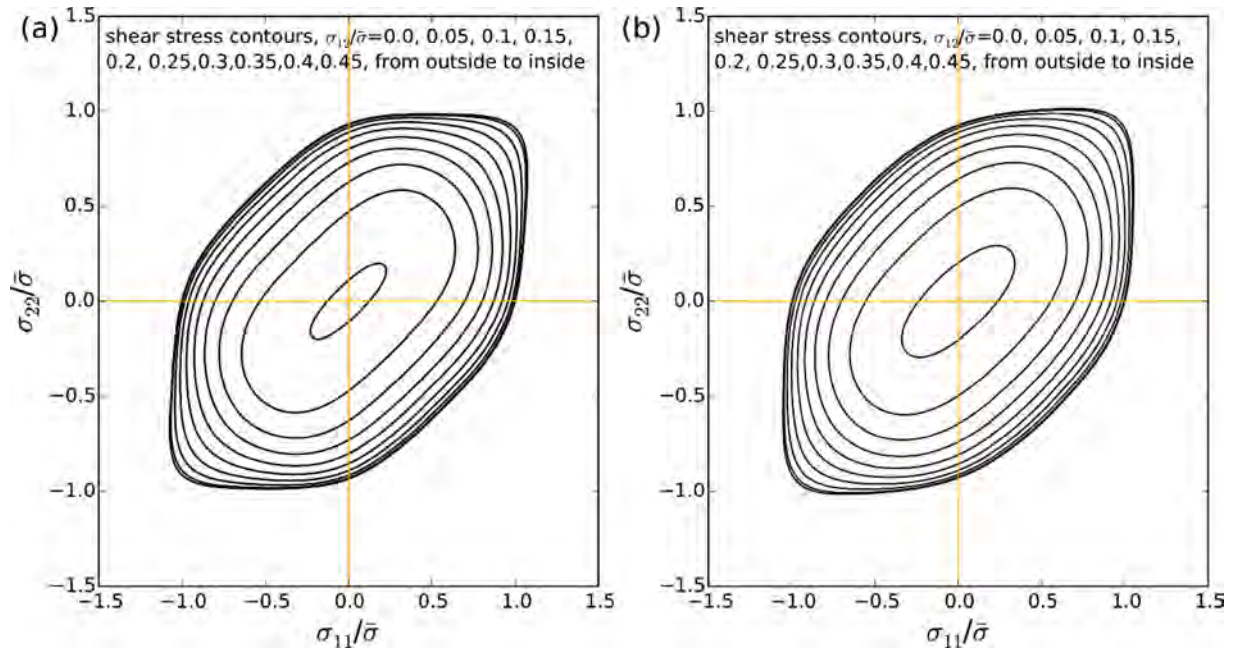

Fig. 10. Yield surfaces obtained for complete texture by fitting to the CP data (a) Yld2000-2D (b) Yld2004-18p.

are used for the former two groups and kept constant throughout the simulation. In the third group, the yield functions were calibrated with the CP data and regularly updated according to the updating criterion.

All the FEM simulations were performed with a single processor of an eight-core Intel Xeon E5-2687W (3.10 GHz). As for the CP-spectral based virtual experiments, eight threads are used. The simulations without updating the plastic anisotropy required about two hours. The simulations with updating the Yld2000-2D yield function starting from the central layer texture and the complete texture required 72 and 77 h, respectively. The simulations with updating the Yld2004-18p yield

function starting from the central layer texture and complete texture required 70 and 77.5 h, respectively. During the stage of the plastic anisotropy updates, it takes ~20 s to update the texture, ~25 s to perform four virtual experiments needed for the calibration of Yld2000-2D, and ~45 s to perform twelve virtual experiments needed for the calibration of Yld2004-18p.

Fig. 11 presents the simulated cup profiles using the Yld2000-2D yield function compared to the experimental data (Yoon et al., 2000). The measured cup profile slightly deviates from orthotropic symmetry. The reason for this may be that a little shift of the circular blank
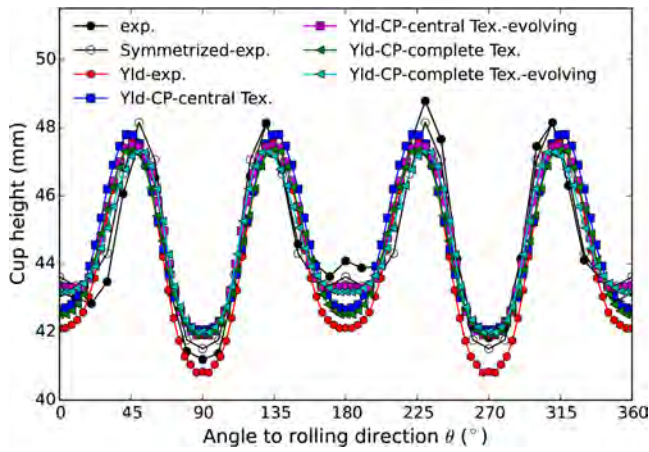
Fig. 11. Comparison of experimental (exp.) and predicted cup profiles of 2090-T3 with Yld2000-2D. Yld-exp.: simulation with non-evolving yield function fitted to experimental data; Yld-CP-central Tex.: simulation with non-evolving yield function fitted to CP data for central layer texture; Yld-CP-central Tex.-evolving: simulation with evolving yield function starting from central layer texture; Yld-CP-complete Tex.: simulation with non-evolving yield function fitted to CP data for complete texture; Yld-CP-complete Tex.-evolving: simulation with evolving yield function starting from complete texture.

Table 4
Average errors between the simulated cup heights and the symmetrized experimental data.

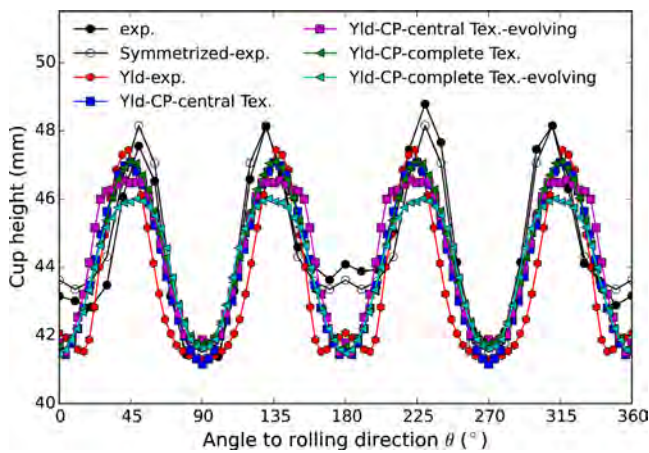|	Fitted to experimental data	Fitted to CP data			
		Central layer texture		Complete texture	
		Non-evolving	Evolving	Non-evolving	Evolving
Yld2000-2D	2.01%	1.80%	1.10%	1.65%	0.93%
Yld2004-18p	3.10%	2.03%	2.20%	1.81%	2.14%

Fig. 12. Comparison of experimental (exp.) and predicted cup profiles of 2090-T3 with Yld2004-18p. Yld-exp.: simulation with non-evolving yield function fitted to experimental data; Yld-CP-central Tex.: simulation with non-evolving yield function fitted to CP data for central layer texture; Yld-CP-central Tex.-evolving: simulation with evolving yield function starting from central layer texture; Yld-CP-complete Tex.: simulation with non-evolving yield function fitted to CP data for complete texture; Yld-CP-complete Tex.-evolving: simulation with evolving yield function starting from complete texture.

occurred during the drawing experiment, resulting in a deviation of the center of the blank from the central axis. To have a better comparison of the experimental and the predicted results, the symmetrized experimental cup profile is therefore also presented in the figure. The simulations conducted with the evolving Yld2000-2D predict all six ears of the cup profile seen in the experiment, while simulations with a constant Yld2000-2D predict only four ears. It can be seen that the predicted cup profiles with evolving yield functions are in better agreement with the symmetrized experimental cup profile than with the original measured cup profile. Table 4 lists the average errors between the simulated cup heights and the symmetrized experimental data. As it can be seen from the Table 4, simulations with evolving Yld2000-2D have smaller average errors than simulations with non-evolving Yld2000-2D, which is consistent with the observation in Fig. 11. Moreover, the average errors of the simulations for the complete texture are slightly smaller than those of the simulations for the central layer texture. However, the simulated cup heights at 0°, 45°, 135°, 180°, 225°, and 315° with evolving Yld2000-2D for the central layer texture agree slightly better than those of the complete texture.

Fig. 12 depicts the simulated cup profiles with the Yld2004-18p yield function compared to the experimental data. The simulation with the yield function calibrated with the experimental data predicts, in agreement with the experiment, six ears. In contrast, the results obtained with the Yld2004-18p yield function calibrated with CP data deviate significantly at 180° and 0°/360° from the experimental results. The simulated cup heights with the evolving Yld2004-18p yield function around 45°, 135°, 225°, and 315° are deteriorated compared to that with the constant yield function. In Table 4, the average errors for simulations with evolving Yld2004-18p are also larger than those for simulations with non-evolving Yld2004-18p. Nevertheless, small ears around 0° (or 360°) and 180° are still captured in the simulation starting from the central layer texture. Though simulations with both textures do not agree well with the experiment, the cup heights at 0°, 45°, 135°, 180°, 225°, and 315° predicted with the simulation based on the central layer texture still show a litter better results than those predicted with the simulation starting from the complete texture. However, similar to the simulations using Yld2000-2D yield function, the simulations with the complete texture also have slightly smaller average errors than those of the simulations with the central layer texture.

Fig. 13 shows the final configuration of the drawn cup simulated with the evolving Yld2000-2D yield function starting from the central layer texture. Three typical positions (P1, P2, and P3 are located at TD, 45° to RD, and RD, respectively) are indicated in the figure, and the final textures at these positions are also shown in the figure. In comparison with the initial texture (central layer texture shown in Fig. 1(b)), significant texture changes have taken place at the three positions. The final configuration of the drawn cup simulated with the evolving Yld2000-2D starting from the complete texture is shown in Fig. 14. The plastic strain distributions of the drawn cup shown in Figs. 13 and 14 are very similar. The final textures at P1, P2, and P3 shown in Fig. 14 are also similar to those shown in Fig. 13, respectively. Because both the central layer texture and the complete texture include S and Brass components, these texture components will evolve in a similar way at the same position.

Fig. 15 shows the final cup configuration simulated with the evolving Yld2004-18p yield function starting from the central layer texture. The textures at the three indicated positions are consistent with those simulated with the evolving Yld2000-2D yield function, respectively. This also indicates the consistency between the plane stress simulation and the full 3D simulation.

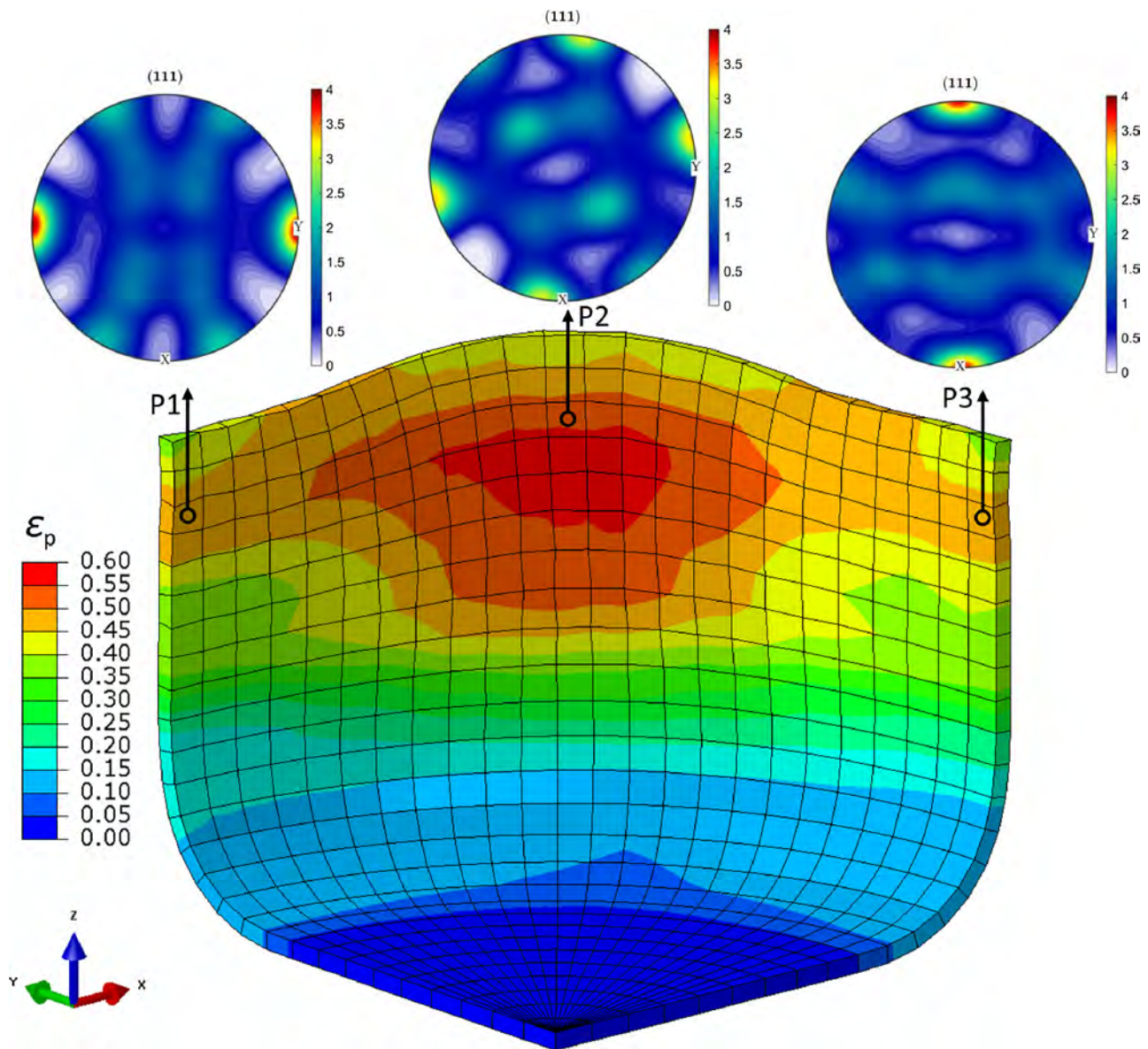Fig. 16 shows the number of yield surface updates for two

Fig. 13. Deformed configuration and equivalent plastic strain (ε_p) distribution of the cup simulated with the evolving Yld2000-2D yield function starting from the central layer texture. The final textures at the three positions indicated are also shown.

simulations starting from the central layer texture. As the anisotropy is updated every five percent of plastic strain, it is obvious that the distribution of the number of updates correlates with that of the plastic strain. The maximum number of updates for the Yld2000-2D yield function is 11 and that for the Yld2004-18p yield function is 9. Because the solid elements have a slightly higher stiffness than the shell elements, the plastic strain level achieved in the simulation with shell elements is higher than that achieved in the simulation with solid elements.

5.3. Evolution of the plastic anisotropy

Figs. 17–19 show the evolution of the plastic anisotropy, represented by the uniaxial yield stresses and *r*-values predicted by the Yld2000-2D yield function, at the positions P1, P2, and P3 of the cup

indicated in Fig. 13, respectively. At point P1, the largest yield stress always occurs at 90°, and it becomes larger than the yield stress at 0° as the plastic strain increases. The lowest yield stress occurs at 45° when the plastic strain is below 0.4. When the plastic strain reaches 0.45 the yield stress at 0° becomes the lowest. The *r*-value at 0° has a very slight increase, while the *r*-value at 90° increases by ∼1.0. At point P2, though the largest yield stress still occurs at 90°, the yield stresses at 0° and 90° become nearly identical when the plastic strain reaches 0.5. The lowest yield stress always occurs at 45°. The shape of the normalized yield stress versus θ is nearly symmetric to 45° when the plastic strain reaches 0.5. The *r*-value at 45° decreases by ∼0.6, while the *r*-values at 0° and 90° increase where the increase at 0° is higher. As a result, the plastic anisotropy in terms of *r*-value weakens, i.e., the material at this point evolves towards more isotropic behavior. At point P3, the largest yield stress occurs at 90° when the plastic strain is
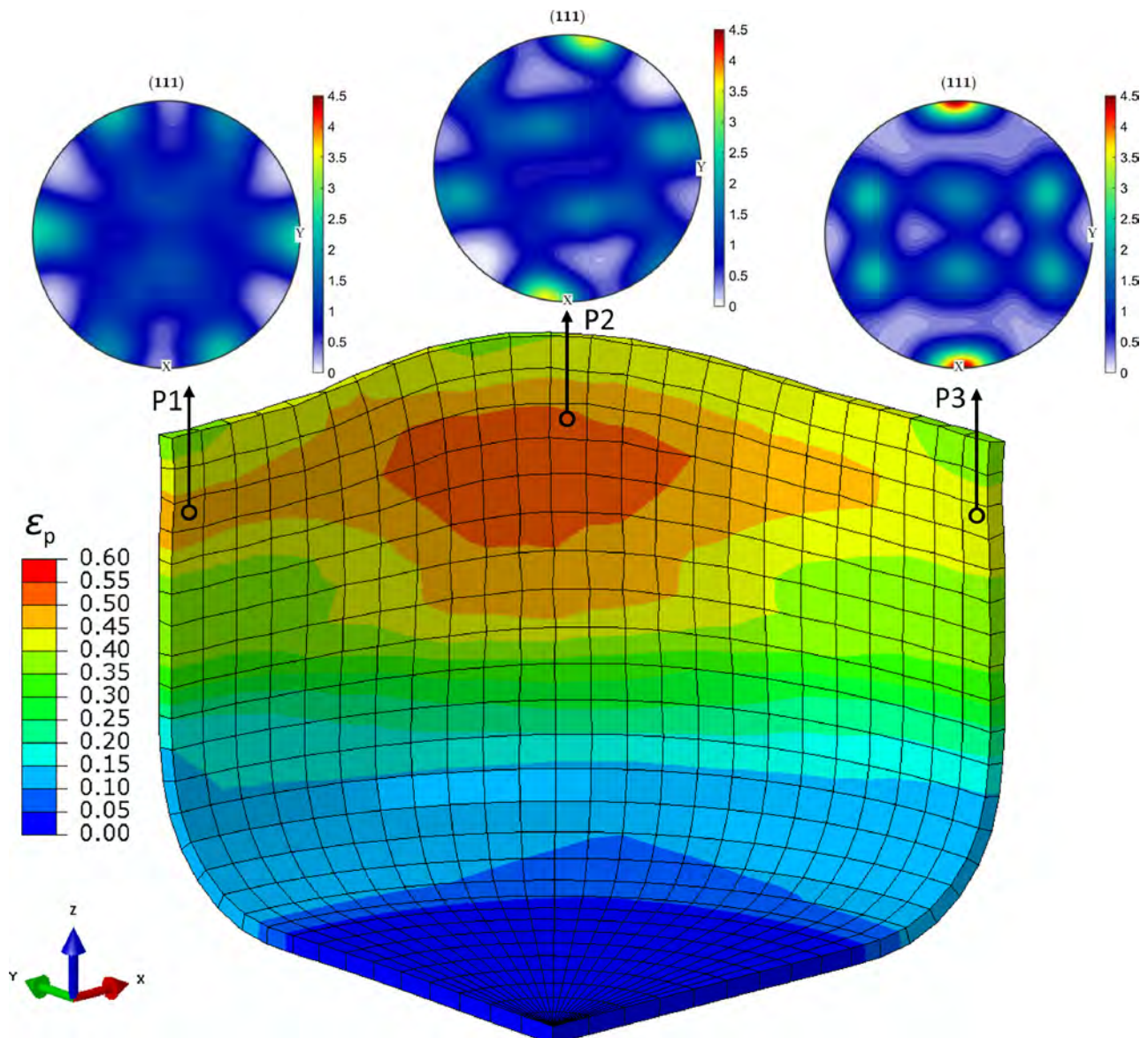
Fig. 14. Deformed configuration and equivalent plastic strain (ε_p) distribution of the cup simulated with the evolving Yld2000-2D yield function starting from the complete texture. The final textures at the three positions indicated are also shown.

smaller than 0.2. When the plastic strain exceeds 0.2 the yield stress at 0° becomes the largest. The lowest yield stress still occurs at 45°. The *r*-value at 0° increases from 0.18 to 0.57, and the *r*-value at 90° decreases from 0.46 to 0.37, while the *r*-value at 45° decreases first and then increases again.

Fig. 20 depicts the evolution of the yield locus at the three positions. The change of the shape of the yield locus is quite obvious. The yield locus at point P1 expands compared to the initial one, while that at point P3 shrinks. The change of the yield locus at point P2 is relatively small in comparison with that at P1 and P3. The normal directions of the yield loci also show some deviation from the original ones. It is clear that considerable anisotropy changes have taken place at all the three positions. In addition, from the comparison of the anisotropy evolution behavior at the three positions, it can be seen that the anisotropy

evolution at various positions of the cup is quite different. The parameters of the Yld2000-2D yield function at point P1 during the cup drawing simulation starting from the central layer texture are listed in Table 5 as an example, documenting the gradual changes in these parameters.

Fig. 21 shows the evolution of the plastic anisotropy at point P3 of the cup simulated with the evolving Yld2000-2D starting from the complete texture. The yield stress at 90° becomes much smaller than that at 0° with increasing plastic strain. The *r*-value at 0° increases from 0.41 to 0.79, and the *r*-value at 45° increases from 1.9 to 2.5, while the *r*-value at 90° decreases slightly. The yield locus also shrinks with increasing plastic strain. As the components of the complete texture and the central layer texture are different, the evolutions of plastic anisotropy also exhibit different behaviors.
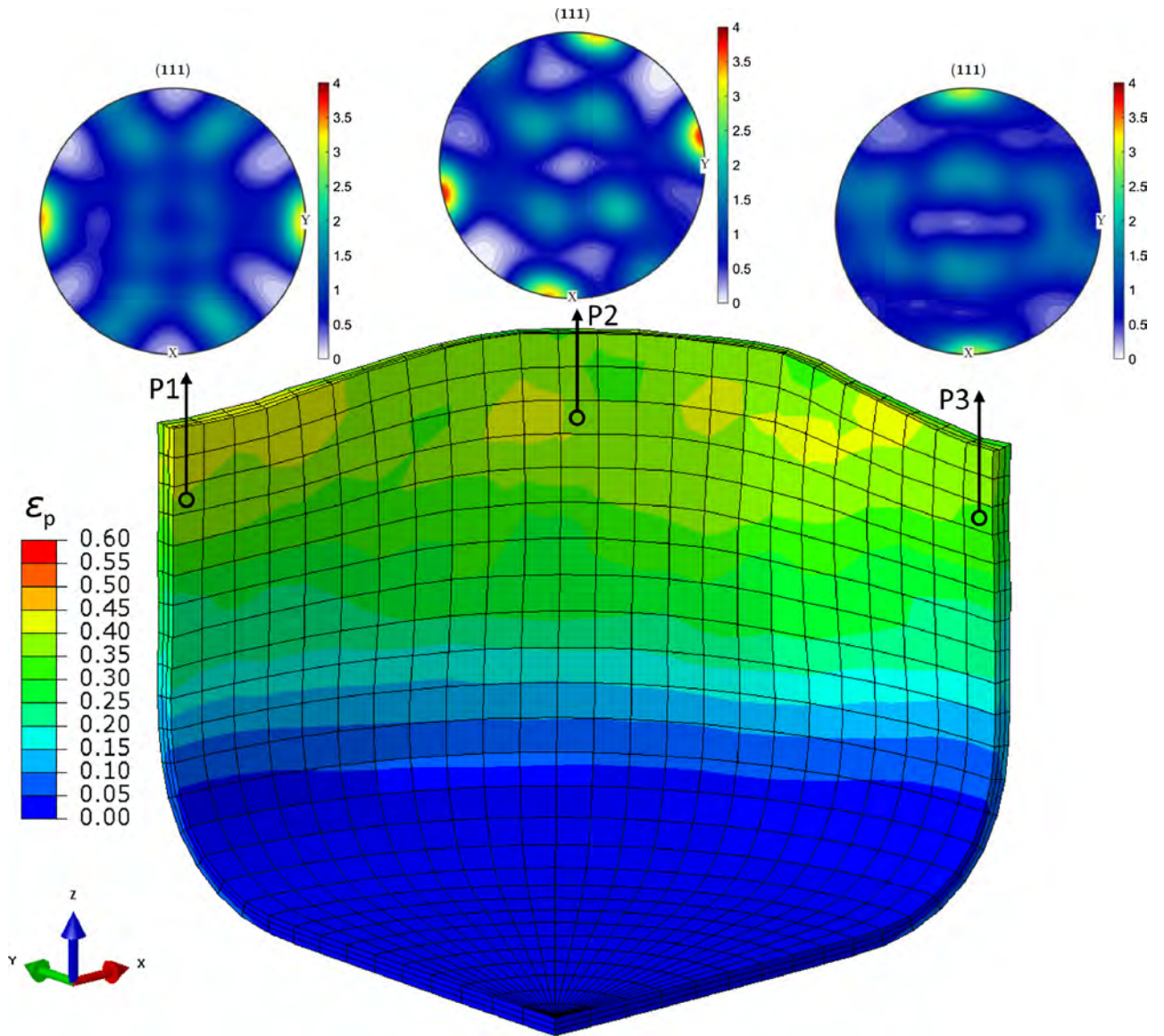
Fig. 15. Deformed configuration and equivalent plastic strain (ε_p) distribution of the cup simulated with the evolving Yld2004-18p yield function starting from the central layer texture. The final textures at the three positions indicated are also shown.
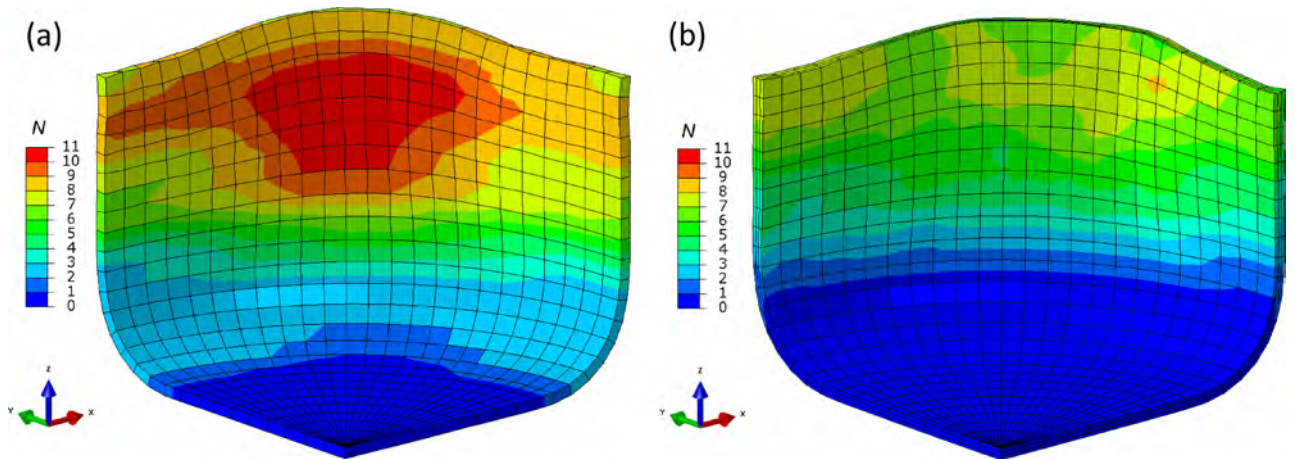

Fig. 16. Number (*N*) of yield surface updates for the simulations starting from the central layer texture (a) Yld2000-2D (b) Yld2004-18p.
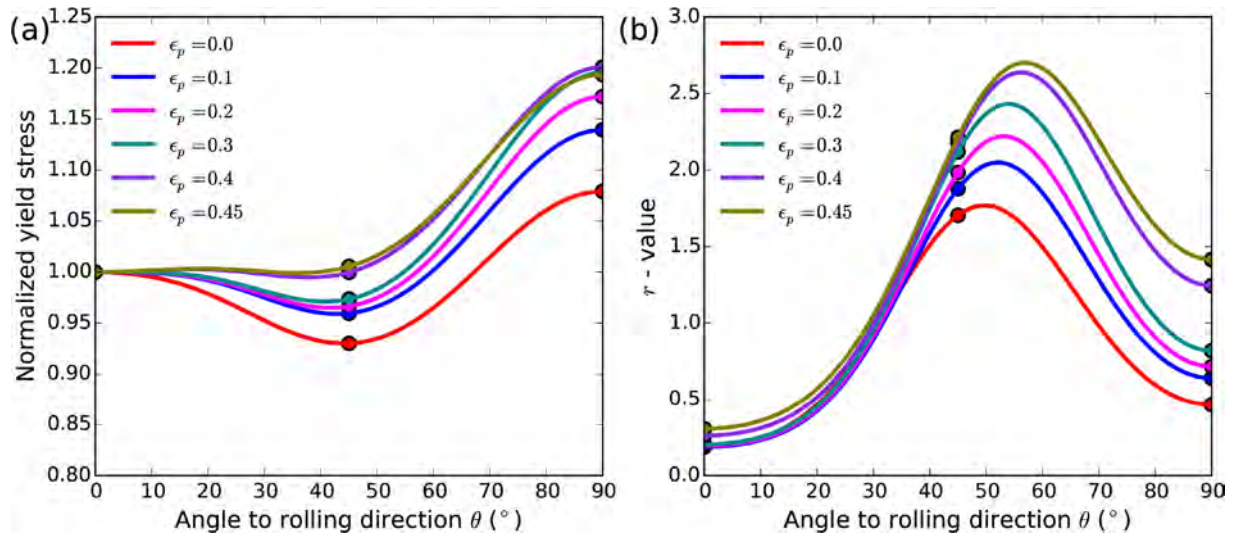
Fig. 17. Evolution of the plastic anisotropy at point P1 of the cup simulated with the evolving Yld2000-2D yield function starting from the central layer texture. (a) Normalized yield stress versus θ (b) r-value versus θ. ε_p is the equivalent plastic strain. The symbols are the data points obtained from the corresponding virtual experiments.
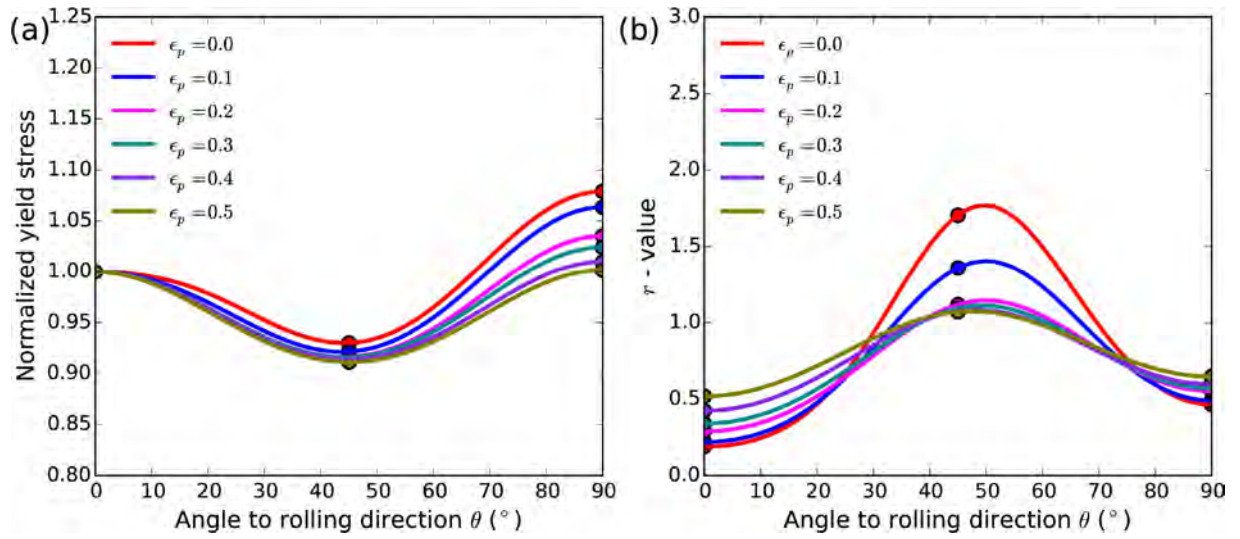

Fig. 18. Evolution of the plastic anisotropy at point P2 of the cup simulated with the evolving Yld2000-2D yield function starting from the central layer texture. (a) Normalized yield stress versus θ; (b) r-value versus θ. ε_p is the equivalent plastic strain. The symbols are the data points obtained from the corresponding virtual experiments.
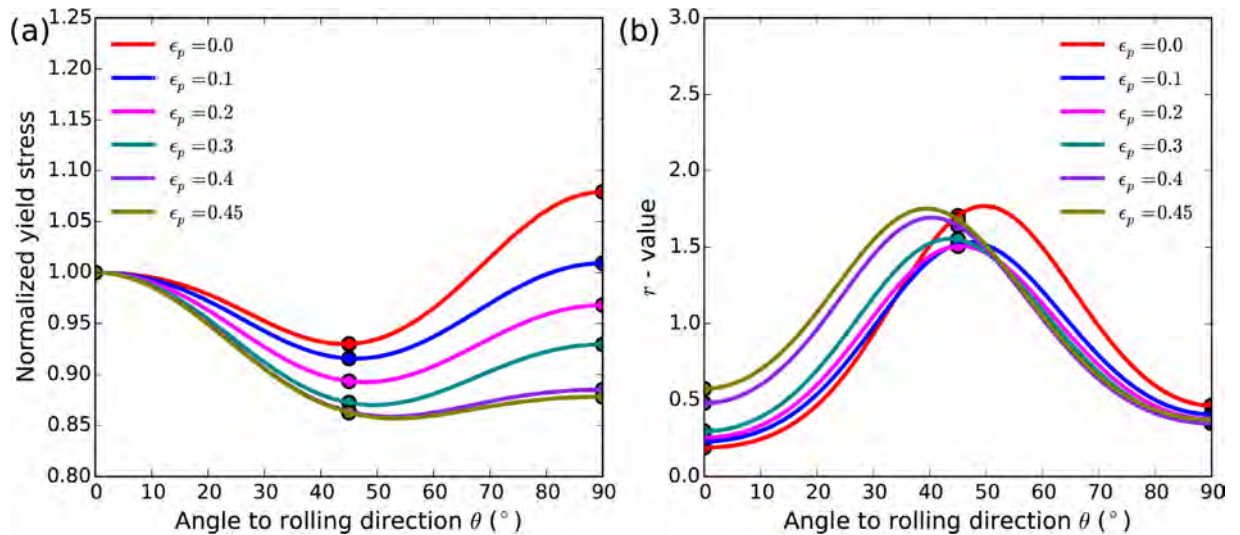

Fig. 19. Evolution of the plastic anisotropy at point P3 of the cup simulated with the evolving Yld2000-2D yield function starting from the central layer texture. (a) Normalized yield stress versus θ (b) r-value versus θ. ε_p is the equivalent plastic strain. The symbols are the data points obtained from the corresponding virtual experiments.
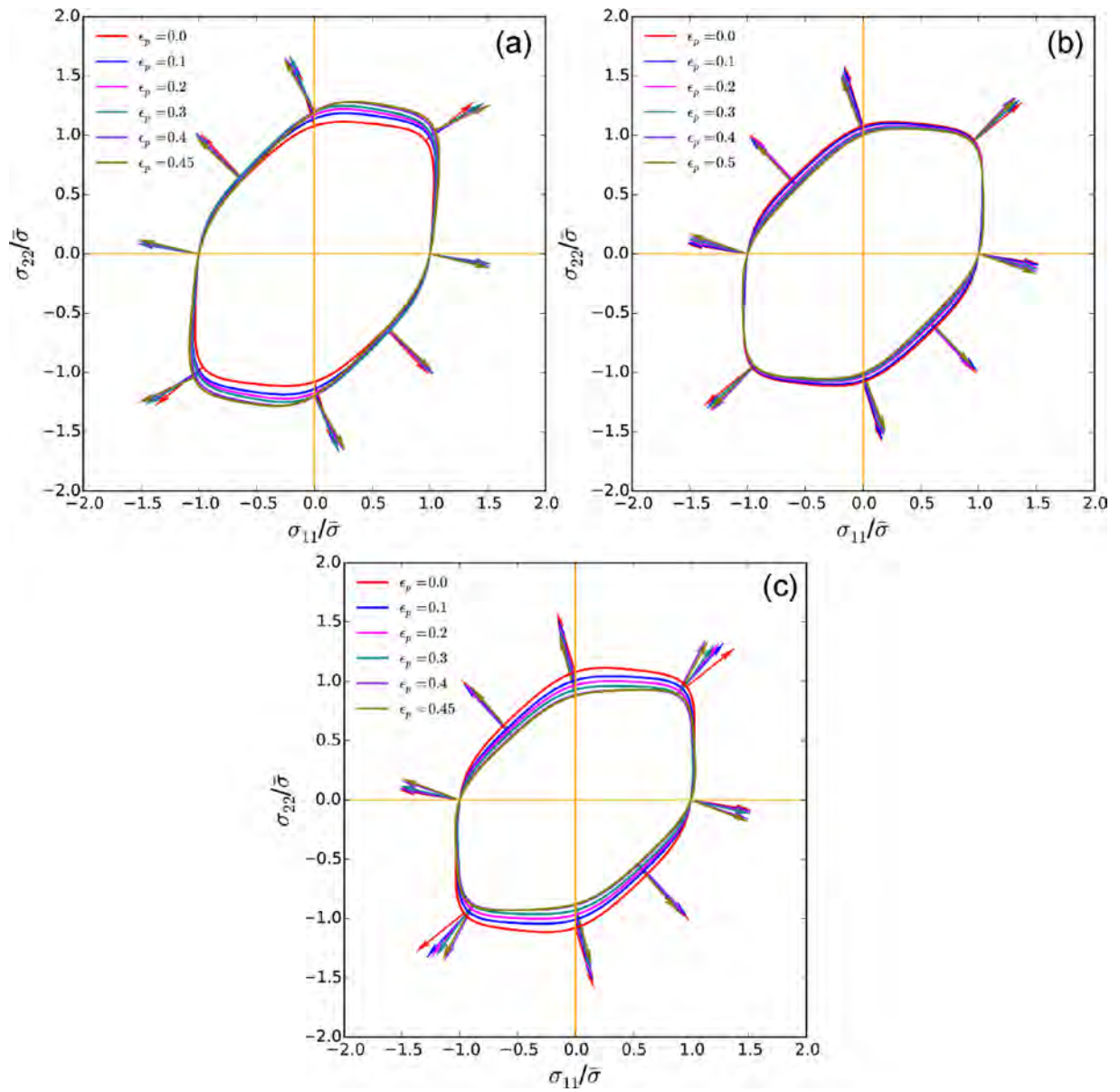
Fig. 20. Evolution of the plastic anisotropy (yield locus at different equivalent plastic strains ε_p) of the cup simulated with the evolving Yld2000-2D yield function starting from the central layer texture at three positions (a) P1 (b) P2 (c) P3.

Table 5
Evolving parameters of Yld2000-2D yield function at point P1 during the cup drawing simulation starting from the central layer texture (exponent $n = 8$). ε_p in the table is the equivalent plastic strain.

| ε_p	α_1	α_2	α_3	α_4	α_5	α_6	α_7	α_8
0.05	0.75091	0.96174	1.15007	0.97392	1.04969	0.97155	1.09759	1.00697
0.10	0.73634	0.95009	1.13876	0.94216	1.04249	0.93697	1.07801	0.97948
0.15	0.74542	0.93053	1.13745	0.92849	1.04032	0.92812	1.07352	0.97161
0.20	0.76882	0.90361	1.13796	0.92018	1.04036	0.93098	1.07323	0.96567
0.25	0.79198	0.88042	1.13546	0.91269	1.04093	0.93663	1.07346	0.96016
0.30	0.80224	0.86826	1.13397	0.90279	1.03919	0.93099	1.06881	0.94624
0.35	0.81957	0.86269	1.11231	0.88350	1.03309	0.91131	1.05103	0.92668
0.40	0.85133	0.85919	1.10280	0.87804	1.02901	0.90626	1.04234	0.90959
0.45	0.87998	0.85596	1.06771	0.87022	1.02171	0.88923	1.03656	0.91204
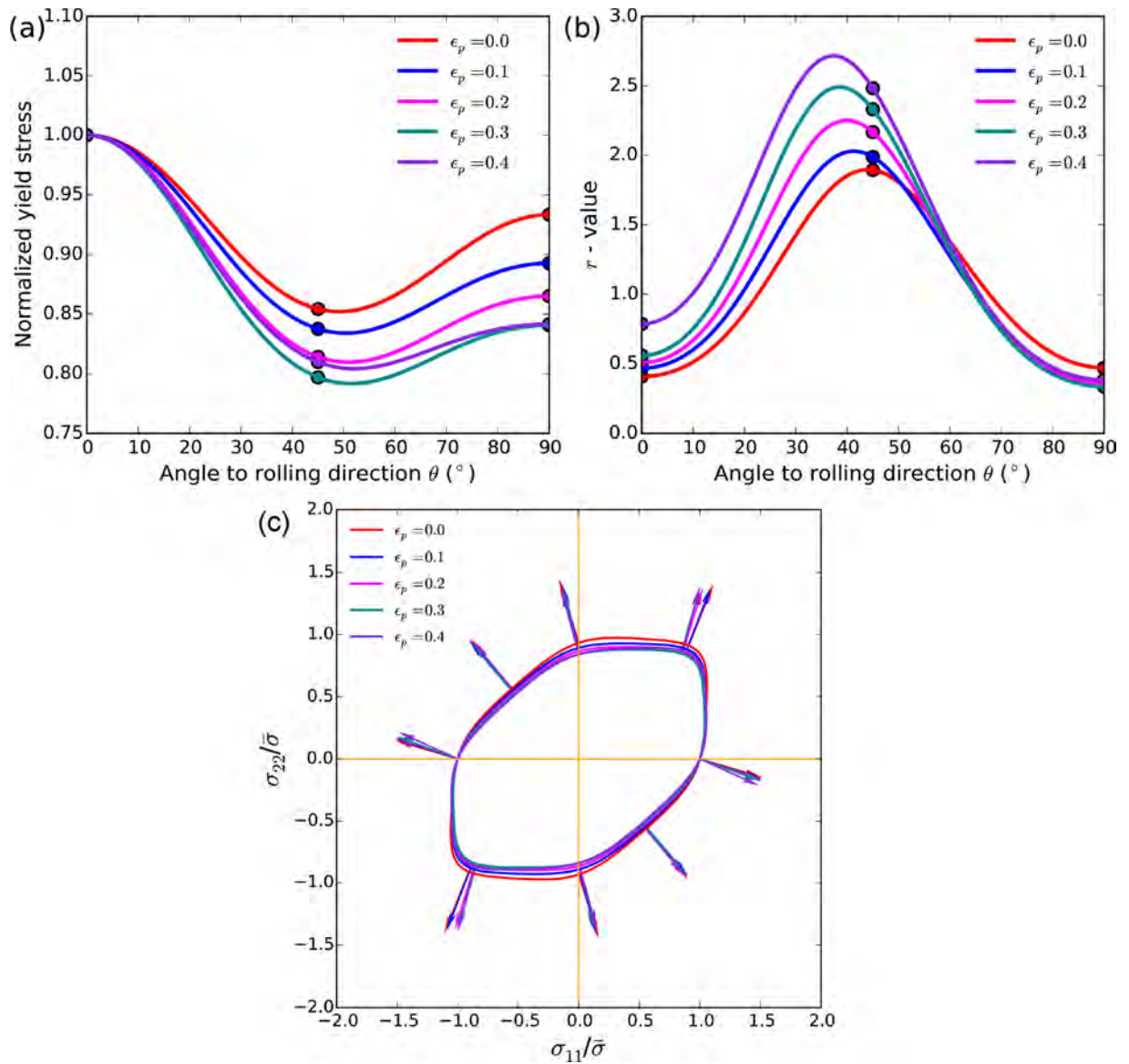
Fig. 21. Evolution of the plastic anisotropy at point P3 of the cup simulated with the evolving Yld2000-2D yield function starting from the complete texture. (a) Normalized yield stress versus θ (b) r-value versus θ (c) yield locus. ε_p is the equivalent plastic strain. The symbols are the data points obtained from the corresponding virtual experiments.

Fig. 22 shows the evolution of the plastic anisotropy at point P3 of the cup simulated with the evolving Yld2004-18p yield function starting from the central layer texture. Compared to the simulation with evolving Yld2000-2D yield function, it can capture more details of the anisotropic properties of the yield stress and r-value. The evolution of the plastic anisotropy at the same point of the cup simulated with the evolving Yld2004-18p starting from the complete texture is also shown in Fig. 23. It also provides more detailed information on the evolution of plastic anisotropy for the simulation starting from the complete texture.

Although the thickness of the sheet is small, the evolution of plastic anisotropy across the thickness direction is not identical among the different through-thickness layers. The evolution of the plastic anisotropy of the three integration points across the thickness direction

located at P3 of the simulation with evolving Yld2000-2D starting from the central layer texture is shown in Fig. 24. At a plastic strain of 0.1, the yield stress profile and r-value profile at the three integration points are almost identical, while differences clearly emerge at larger plastic strains. This can be ascribed to the fact that the material near the top of the blank is in tension while the material near the bottom is in compression during bending. The final textures across the thickness are shown in Fig. 25, revealing the differences among the through-thickness layers.

The finding that the evolving Yld2004-18p does not provide better predictions than the evolving Yld2000-2D is surprising. The reason for this might be the systematic error introduced by neglecting the strong texture gradient of the 2090-T3 aluminum alloy sheet across the thickness direction in the simulation. As Yld2004-18p has more
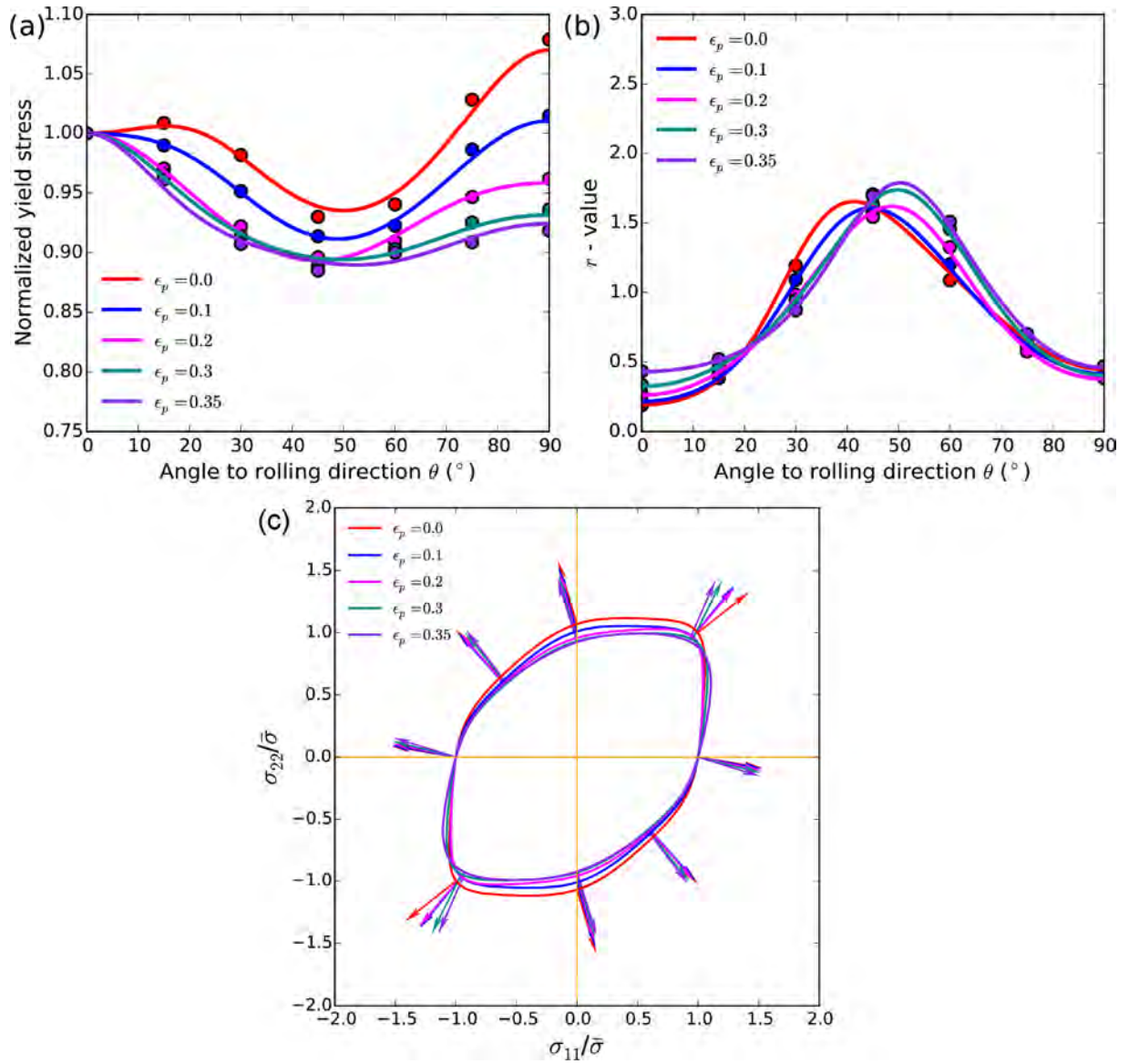
Fig. 22. Evolution of the plastic anisotropy at point P3 of the cup simulated with the evolving Yld2004-18p yield function starting from the central layer texture. (a) Normalized yield stress versus θ (b) r-value versus θ (c) yield locus. ε_p is the equivalent plastic strain. The symbols are the data points obtained from the corresponding virtual experiments.

parameters than Yld2000-2D, the former is able to capture more detailed information on the plastic anisotropy than Yld2000-2D. Accordingly, the systematic error may be magnified by the more advanced anisotropic yield function when the plastic anisotropy is passed from the CP model to the yield function. However, this finding does not mean that more advanced anisotropic yield functions are in general not suitable to be applied in the present multi-scale framework. If the RVE is highly representative for the material, and the CP model is accurate enough, more advanced anisotropic yield functions should in general perform better. Additionally, employing multiple RVEs assigned with different textures across the thickness direction (e.g., surface, sub-surface and central layer of the sheet) in one simulation may be a

promising way to capture the texture gradient effect of sheet metals (Tikhovskiy et al., 2006, 2008).

6. Conclusions

We presented an approach to update advanced anisotropic yield functions in macroscopic forming simulations by coupling them with microscopic full-field crystal plasticity (CP)-spectral based virtual experiments. The approach has been validated by finite element simulations of a deep drawing test for a 2090-T3 aluminum alloy sheet with two evolving yield functions (Yld2000-2D and Yld2004-18p). Improvement on the prediction of earing has been obtained by the
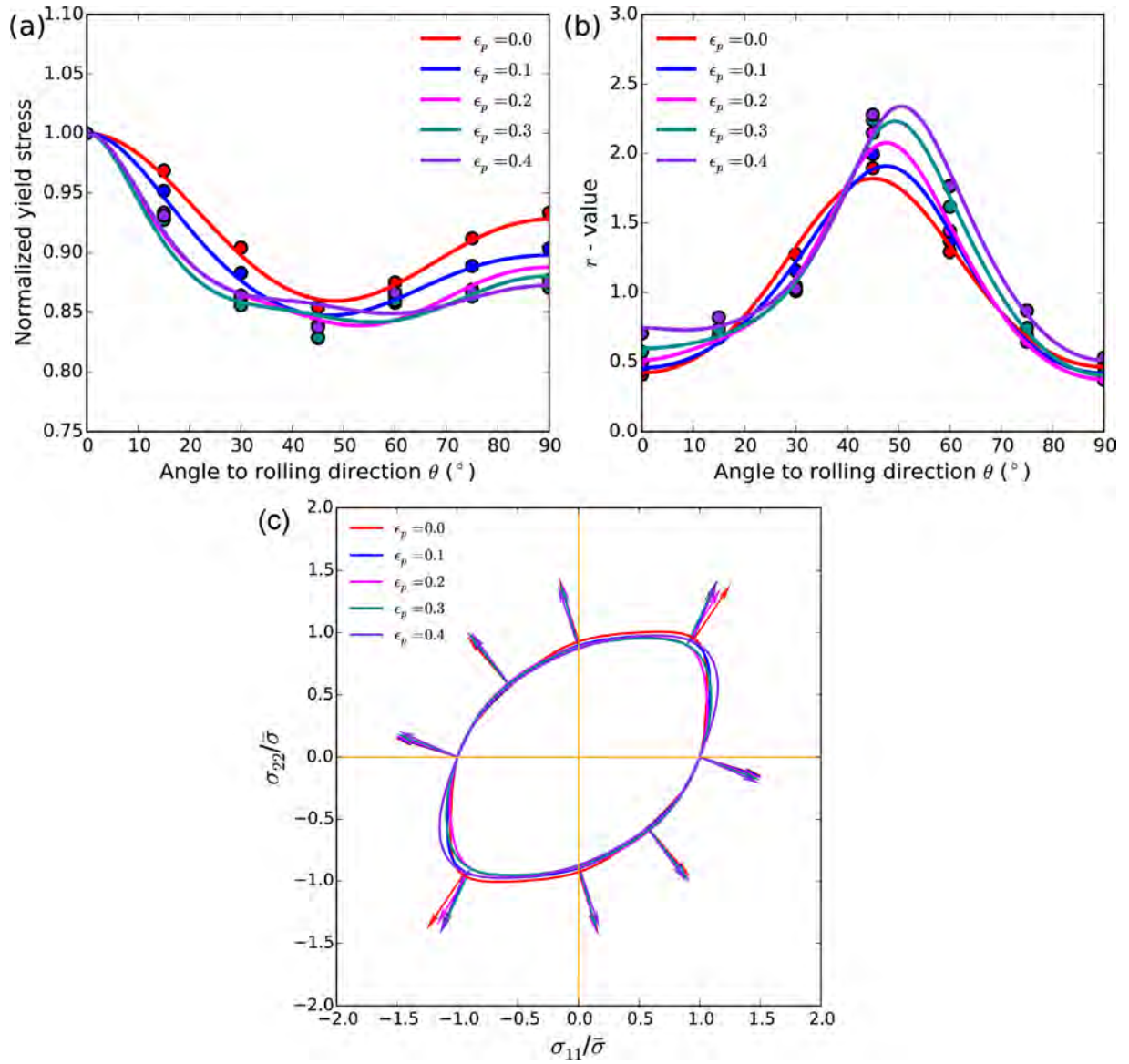
Fig. 23. Evolution of the plastic anisotropy at point P3 of the cup simulated with the evolving Yld2004-18p yield function starting from the complete texture. (a) Normalized yield stress versus θ (b) r-value versus θ (c) yield locus. ε_p is the equivalent plastic strain. The symbols are the data points obtained from the corresponding virtual experiments.

evolving Yld2000-2D yield function. The evolution of the plastic anisotropy during cup drawing has been investigated and we observe a considerable effect on simulation accuracy. Texture evolution at different positions of the cup can be quite different, which implies the same trend for the evolution of anisotropy. Minor differences in the anisotropy evolutions across the thickness of the sheet have been observed. Simulations considering the central layer texture tend to better capture the earing profile while simulations considering the complete texture tend to have smaller average errors of the cup heights.

The approach has been integrated into the DAMASK multi-physics modeling package (https://damask.mpie.de/) to realize a novel multi-scale modeling framework that overcomes limitations of established homogenization schemes. In future, the capabilities of this approach can be exploited to predict the behavior of more complex materials such as dual phase steels (Tasan et al., 2015), which impose severe challenges on classical homogenization schemes. Moreover, more advanced CP constitutive formulations implemented in DAMASK are available for use in the multi-scale model. This allows to select models that are parameterized by lower scale simulations (Wong et al., 2016) and require even less experimental efforts. Finally, it should be noted that the presented framework can be used in conjunction with other yield functions and can be applied to forming processes that are more complex than cup drawing which had been chosen here as a demonstrator case.
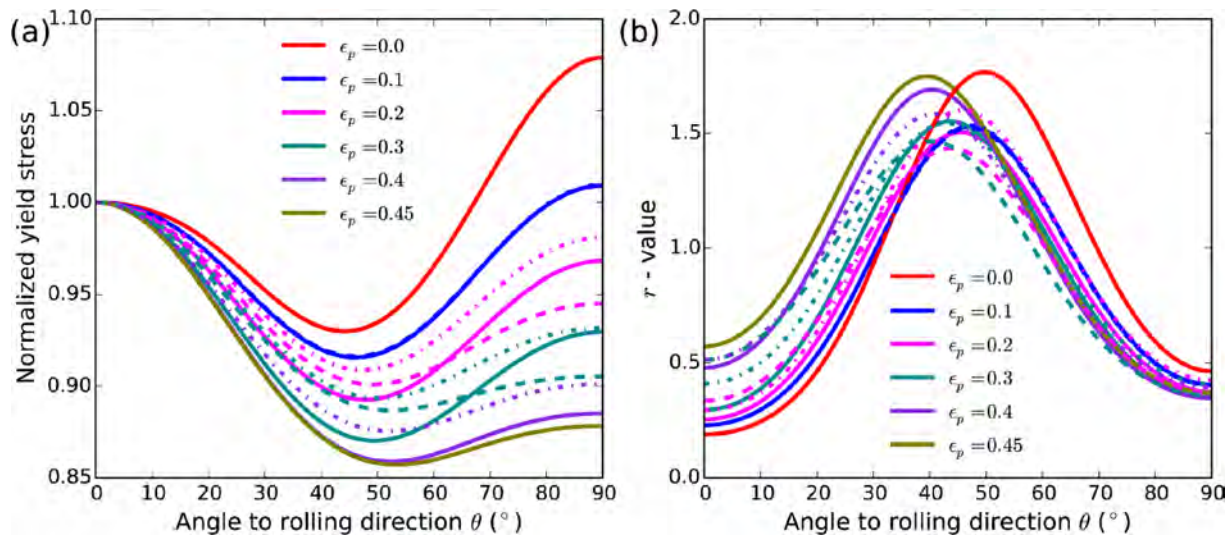
Fig. 24. Evolutions of the plastic anisotropy across the thickness at the position P3 of the sheet in the simulation with the evolving Yld2000-2D yield function starting with the central layer texture. ε_p is the equivalent plastic strain. The solid lines are the results of the integration point at the top. The dashed lines are the results of the integration point in the middle. The dash-dot lines are the results of the integration point at the bottom.
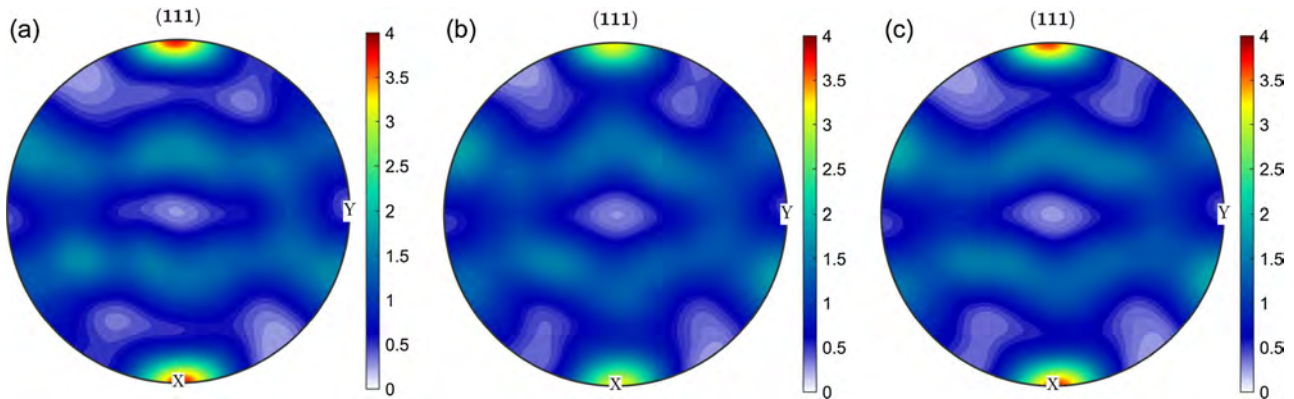

Fig. 25. Final textures across the thickness at the position P3 of the sheet for the simulation with the evolving Yld2000-2D yield function starting with the central layer texture. (a) top (b) middle (c) bottom integration point.

Acknowledgments

References

An, Y., Vegter, H., Carless, L., Lambriks, M., 2011. A novel yield locus description by combining the Taylor and the relaxed Taylor theory for sheet steels. Int. J. Plast. 27, 1758–1780.

Bachmann, F., Hielscher, R., Schaeben, H., 2010. Texture analysis with MTEX–free and open source software toolbox, solid state phenomena. Trans. Tech. Public. 63–68.

Barlat, F., Aretz, H., Yoon, J.-W., Karabin, M., Brem, J., Dick, R., 2005. Linear transformation-based anisotropic yield functions. Int. J. Plast. 21, 1009–1039.

Barlat, F., Brem, J., Yoon, J., Chung, K., Dick, R., Lege, D., Pourboghrat, F., Choi, S.-H., Chu, E., 2003. Plane stress yield function for aluminum alloy sheets-part 1: theory. Int. J. Plast. 19, 1297–1319.

Barlat, F., Brem, J.C., Liu, J., 1992. On crystallographic texture gradient and its mechanical consequence in rolled aluminum-lithium sheet. Scr. Metall. Mater. 27, 1121–1126.

Barlat, F., Gracio, J.J., Lee, M.-G., Rauch, E.F., Vincze, G., 2011. An alternative to kinematic hardening in classical plasticity. Int. J. Plast. 27, 1309–1327.

Barlat, F., Lian, K., 1989. Plastic behavior and stretchability of sheet metals. Part I: a yield function for orthotropic sheets under plane stress conditions. Int. J. Plast. 5, 51–66.

Bishop, J., Hill, R., 1951. XLVI. A theory of the plastic distortion of a polycrystalline aggregate under combined stresses. London Edinburgh Dublin Philos. Mag. J. Sci. 42, 414–427.

Comsa, D.-S., Banabic, D., 2008. Plane-stress yield criterion for highly-anisotropic sheet metals. Numisheet 2008 43–48 Interlaken, Switzerland.

Drucker, D.C., 1949. Relation of experiments to mathematical theories of plasticity. J. Appl. Mech.-Trans. Asme 16, 349–357.

Eisenlohr, P., Diehl, M., Lebensohn, R.A., Roters, F., 2013. A spectral method solution to crystal elasto-viscoplasticity at finite strains. Int. J. Plast. 46, 37–53.

Gawad, J., Banabic, D., Van Bael, A., Comsa, D.S., Gologanu, M., Eyckens, P., Van Houtte, P., Roose, D., 2015. An evolving plane stress yield criterion based on crystal plasticity virtual experiments. Int. J. Plast. 75, 141–169.

Gawad, J., Van Bael, A., Eyckens, P., Samaey, G., Van Houtte, P., Roose, D., 2013. Hierarchical multi-scale modeling of texture induced plastic anisotropy in sheet forming. Comput. Mater. Sci. 66, 65–83.

Grytten, F., Holmedal, B., Hopperstad, O., Børvik, T., 2008. Evaluation of identification methods for YLD2004-18p. Int. J. Plast. 24, 2248–2277.

He, W., Zhang, S., Prakash, A., Helm, D., 2014. A hierarchical multi-scale model for hexagonal materials taking into account texture evolution during forming simulation. Comput. Mater. Sci. 82, 464–475.

Hill, R., 1948. A theory of the yielding and plastic flow of anisotropic metals. Proc. R. Soc. London A 193, 281–297.

Hosford, W., 1972. A generalized isotropic yield criterion. J. Appl. Mech. 39, 607–609.

Hosford, W.F., 1979. On yield loci of anisotropic cubic metals. Proceedings of the Seventh North American Metal Working Conference SME 191–197.

Inal, K., Mishra, R.K., Cazacu, O., 2010. Forming simulation of aluminum sheets using an anisotropic yield function coupled with crystal plasticity theory. Int. J. Solids Struct. 47, 2223–2233.

Kohar, C.P., Bassani, J.L., Brahme, A., Muhammad, W., Mishra, R.K., Inal, K., 2019. A new multi-scale framework to incorporate microstructure evolution in phenomenological plasticity: theory, explicit finite element formulation, implementation and validation. Int. J. Plast. 117, 122–156.

Lebensohn, R., Tomé, C., 1993. A study of the stress state associated with twin nucleation and propagation in anisotropic materials. Philos. Mag. A 67, 187–206.

Lin, J., Yang, J., 1999. GA-based multiple objective optimisation for determining

viscoplastic constitutive equations for superplastic alloys. Int. J. Plast. 15, 1181–1196.

Mises, Rv., 1928. Mechanik der plastischen Formänderung Von Kristallen. ZAMM-J. Appl. Math. Mech. 8, 161–185.

Nixon, M.E., Cazacu, O., Lebensohn, R.A., 2010. Anisotropic response of high-purity α-titanium: experimental characterization and constitutive modeling. Int. J. Plast. 26, 516–532.

Peirce, D., Asaro, R., Needleman, A., 1982. An analysis of nonuniform and localized deformation in ductile single crystals. Acta Metall. 30, 1087–1119.

Plunkett, B., Lebensohn, R.A., Cazacu, O., Barlat, F., 2006. Anisotropic yield function of hexagonal materials taking into account texture development and anisotropic hardening. Acta Mater. 54, 4159–4169.

Raabe, D., 1995. Texture simulation for hot rolling of aluminium by use of a Taylor model considering grain interactions. Acta Metall. Mater. 43, 1023–1028.

Rabahallah, M., Balan, T., Bouvier, S., Bacroix, B., Barlat, F., Chung, K., Teodosiu, C., 2009. Parameter identification of advanced plastic strain rate potentials and impact on plastic anisotropy prediction. Int. J. Plast. 25, 491–512.

Raemy, C., Manopulo, N., Hora, P., 2017. On the modelling of plastic anisotropy, asymmetry and directional hardening of commercially pure titanium: a planar Fourier series based approach. Int. J. Plast. 91, 182–204.

Raphanel, J., Van Houtte, P., 1985. Simulation of the rolling textures of bcc metals by means of the relaxed taylor theory. Acta Metall. 33, 1481–1488.

Roters, F., Diehl, M., Shanthraj, P., Eisenlohr, P., Reuber, C., Wong, S.L., Maiti, T., Ebrahimi, A., Hochrainer, T., Fabritius, H.O., Nikolov, S., Friák, M., Fujita, N., Grilli, N., Janssens, K.G.F., Jia, N., Kok, P.J.J., Ma, D., Meier, F., Werner, E., Stricker, M., Weygand, D., Raabe, D., 2019. DAMASK – the Düsseldorf Advanced Material Simulation Kit for modeling multi-physics crystal plasticity, thermal, and damage phenomena from the single crystal up to the component scale. Comput. Mater. Sci. 158, 420–478.

Roters, F., Eisenlohr, P., Hantcherli, L., Tjahjanto, D.D., Bieler, T.R., Raabe, D., 2010. Overview of constitutive laws, kinematics, homogenization and multiscale methods in crystal plasticity finite-element modeling: theory, experiments, applications. Acta Mater. 58, 1152–1211.

Rousselier, G., Barlat, F., Yoon, J.W., 2009. A novel approach for anisotropic hardening modeling. Part I: theory and its application to finite element analysis of deep drawing. Int. J. Plast. 25, 2383–2409.

Saai, A., Dumoulin, S., Hopperstad, O.S., Lademo, O.G., 2013. Simulation of yield surfaces for aluminium sheets with rolling and recrystallization textures. Comput. Mater. Sci. 67, 424–433.

Sachs, G., 1929. Zur ableitung einer fliessbedingung, Mitteilungen Der Deutschen Materialprüfungsanstalten. Springer, pp. 94–97.

Shanthraj, P., Eisenlohr, P., Diehl, M., Roters, F., 2015. Numerically robust spectral methods for crystal plasticity simulations of heterogeneous materials. Int. J. Plast. 66, 31–45.

Tasan, C.C., Diehl, M., Yan, D., Bechtold, M., Roters, F., Schemmann, L., Zheng, C., Peranio, N., Ponge, D., Koyama, M., 2015. An overview of dual-phase steels: advances in microstructure-oriented processing and micromechanically guided design. Annu. Rev. Mater. Res. 45, 391–431.

Taylor, G.I., 1938. Plastic strain in metals. J. Inst. Metals 62, 307–324.

Tikhovskiy, I., Raabe, D., Roters, F., 2006. Simulation of the deformation texture of a 17%Cr ferritic stainless steel using the texture component crystal plasticity finite element method considering texture gradients. Scr. Mater. 54, 1537–1542.

Tikhovskiy, I., Raabe, D., Roters, F., 2008. Simulation of earing of a 17% Cr stainless steel considering texture gradients. Mater. Sci. Eng. A 488, 482–490.

Tjahjanto, D., Eisenlohr, P., Roters, F., 2009. A novel grain cluster-based homogenization scheme. Modell. Simul. Mater. Sci. Eng. 18, 015006.

Van Houtte, P., Delannay, L., Samajdar, I., 1999. Quantitative prediction of cold rolling textures in low-carbon steel by means of the LAMEL model. Texture Stress Microstruct. 31, 109–149.

Van Houtte, P., Li, S., Seefeldt, M., Delannay, L., 2005. Deformation texture prediction: from the Taylor model to the advanced Lamel model. Int. J. Plast. 21, 589–624.

Van Houtte, P., Van Bael, A., 2004. Convex plastic potentials of fourth and sixth rank for anisotropic materials. Int. J. Plast. 20, 1505–1524.

Vegter, H., Ten Horn, C., An, Y., Atzema, E.H., Pijlman, H.H., van den Boogaard, T.H., Huétink, H., 2003. Characterisation and modelling of the plastic material behaviour and its application in sheet metal forming simulation. In: Proceedings of COMPLAS VII. CIMNE, Barcelona.

Wong, S.L., Madivala, M., Prahl, U., Roters, F., Raabe, D., 2016. A crystal plasticity model for twinning- and transformation-induced plasticity. Acta Mater. 118, 140–151.

Yoon, J.W., Barlat, F., Chung, K., Pourboghrat, F., Yang, D.Y., 2000. Earing predictions based on asymmetric nonquadratic yield function. Int. J. Plast. 16, 1075–1104.

Zhang, H., Diehl, M., Roters, F., Raabe, D., 2016. A virtual laboratory using high re-solution crystal plasticity simulations to determine the initial yield surface for sheet metal forming operations. Int. J. Plast. 80, 111–138.

Zhang, K., Holmedal, B., Hopperstad, O., Dumoulin, S., 2014. Modelling the plastic ani-sotropy of aluminum alloy 3103 sheets by polycrystal plasticity. Modell. Simul. Mater. Sci. Eng. 22, 075015.

Zhang, K., Holmedal, B., Hopperstad, O., Dumoulin, S., Gawad, J., Van Bael, A., Van Houtte, P., 2015. Multi-level modelling of mechanical anisotropy of commercial pure aluminium plate: crystal plasticity models, advanced yield functions and parameter identification. Int. J. Plast. 66, 3–30.